Cement and Concrete Research 41 (2011) 339–358

Contents lists available at ScienceDirect

Cement and Concrete Research

journal homepage: http://ees.elsevier.com/CEMCON/default.asp

Meso-scale computational modeling of the plastic-damage response of cementitious composites

Sun-Myung Kim, Rashid K. Abu Al-Rub *

Zachry Department of Civil Engineering, Texas A&M University, College Station, TX 77843, USA

ARTICLE INFO

Article history:
Received 1 February 2010
Accepted 14 December 2010

Keywords:
B. Meso-scale analysis
C. Plasticity and Damage
E. Concrete
C. Finite element modeling
B. Interfacial transmission zone

ABSTRACT

Concrete is considered as a 3-phase composite material; mortar matrix, aggregates, and interfacial transmission zone (ITZ). In order to investigate the contribution of each phase to the strength and damage response of concrete, 2-D and 3-D meso-scale simulations based on a coupled plasticity-damage model are carried out. The aggregates are modeled as a linear-elastic material, whereas the mortar matrix and ITZ are modeled using a coupled plasticity-damage model with different tensile and compressive mechanical behavior. Aggregate shape, distribution, and volume fraction are considered as simulated variables. The effect of the ITZ thickness and the strength of the ITZ and mortar matrix are also evaluated. It is shown that the behavior of concrete is merely dependent on the aggregate distribution and the strength of the mortar matrix, but dependent on aggregate shape, size, and volume fraction, and the thickness and strength of the ITZ.

1. Introduction

Concrete can be considered as a three-phase composite material consisting of mortar matrix, aggregate, and interfacial transition zone (ITZ) between the aggregate and the mortar matrix. However, the majority of the conducted research on the inelastic and damage behavior of concrete materials and structures has been focused on treating concrete as a homogeneous material at the macroscopic scale which did not allow one to establish the microstructure–property relationship for designing better and superior fracture-resistant cementitious materials. Micromechanical modeling of the inelastic and damage behavior of each phase in the concrete material is not a trivial task since: [1] the properties of the ITZ, which plays a very important role in the concrete fracture behavior, are not easy to be measured experimentally; and [2] the computational cost is very high. However, due to the recent advances in understanding the chemical composition, thickness, and strength of the ITZ and the developments in computational power, one can effectively simulate the micro-mechanical behavior of concrete materials in order to get insights about the effect of various microstructural features (e.g. aggregate size, shape, gradation, and distribution, ITZ thickness and mechanical properties, the mortar mechanical properties, etc.). This will ultimately guide the design of better and superior fracture resistant concrete materials and structures. Therefore, this study is focused on conducting such a desirable micromechanical study using a recently developed coupled plasticity-damage model by Cicekli et al. [12].

The mesoscopic level analysis considering concrete as a composite material is the most practical and useful method for evaluating the composite behavior of concrete. The process of the mesoscale analysis can be categorized mainly into two steps. First step is to generate the 2-D or 3-D particles taking into account the shape, distribution, and volume fraction of aggregates, and second one is to perform a simulation with FE software applying constitutive models to each phase. The generation of the particles is one of the important research topics, and several modeling techniques have been proposed: [1] the random two-dimensional natural shape aggregate model [50]; [2] the random particle model [6]; [3] the beam lattice model [37,44]; [4] the random packing particle model [16]; and [5] the beam-particle model [53]. Although there is no doubt that the various particles generation techniques proposed until now made great progress to the simulation for concrete on mesoscopic level, the generation of the realistic 3-D random distributed actual shape of aggregates model is still a challenging task.

The random two-dimensional natural shape aggregate model proposed by Wittmann et al. [50] is a more realistic mesoscale analysis model than a circular shape aggregate model. The model, however, has a weak point that aggregates are generated one by one. Therefore, an advanced arbitrary shape aggregate generation algorithm, such as the Monte Carlo random sampling principle is proposed from a decade ago in order to overcome this shortcoming [15,22,49]. However, the important micromechanical properties, such as aggregate volume fraction was not included in their papers. The beam lattice model was widely adopted by several researchers in order to investigate the effect of the micromechanical properties on the tensile behavior of concrete [18,21,24–30,37]. Although concrete can be considered as a 3-phase particulate composite, and simplicity is one of the advantages of this

* Corresponding author. Tel.: +1 979 862 6603; fax: +1 979 845 6554.
E-mail address: rabualrub@civil.tamu.edu (R.K. Abu Al-Rub).

0008-8846/$ – see front matter © 2010 Elsevier Ltd. All rights reserved.
doi:10.1016/j.cemconres.2010.12.002

approach, the response of the concrete, however, was too brittle due to the assumption that each lattice beam follows a linear elastic behavior until brittle failure, and a relatively high computational cost is needed. In the beam-particle model introduced by Zhang et al. [53] concrete is considered as a two-phase composite material composed of matrix and aggregates without considering the ITZ. The aggregates were simulated as particle elements, and the particles were linked each other by an elastic-brittle beam element. Therefore, the beam-particle model also showed too brittle behavior.

Although almost all meso-scale analysis of concrete including researches listed above have been performed with two dimensional meso-scale model, several three dimensional meso-scale analyses have also been carried out in order to predict the damage behavior of concrete more precisely. Lilliu and van Mier [24] developed a 3D lattice model in order to solve the problem of brittleness of concrete, and reported that the 3D lattice model represents the more ductile behavior than the 2D lattice model. The thickness of the ITZ in this model, however, is much wider than the real ITZ (at least 10 times as large as the real ITZ). Wriggers and Moftah [51] considered 3-dimensional geometrical models for concrete, and three different sized spherical aggregates were used. However, the model was considered as a two-phase composite with neglecting the ITZ phase that plays an important role in the fracture process. Caballero et al. [8,9] also developed a 3-D meso-structural analysis model under uniaxial and biaxial loading and showed effectively the development of damage. This model, however, used only single sized coarse aggregate.

At the macroscopic level, the crack nucleation and propagation in concrete material under loading is entirely dependent on the direction of principal stresses. At the mesoscopic level, however, the size and distribution of aggregate and the strength of each phase have a significant effect on the damage initiation and crack propagation. Especially, the accurate understanding of the properties and behavior of ITZ is one of the most important issues in the meso-scale analysis because the damage is initiated at the weakest region and the ITZ is generally the weakest link in concrete. Although the characteristic of the ITZ is not clearly understood currently [30,31,38], it can be assumed that the behavior of the ITZ, which has weaker mechanical properties, is similar to that of the mortar matrix but with reduced stiffness and strength. Based on this assumption, the material properties of the mortar matrix and the ITZ should be chosen carefully. Moreover, the aggregate is modeled as a linear elastic material since the aggregate shows more brittle behavior than the mortar matrix, and has a higher Young's modulus and yield strength.

In this paper, two-dimensional meso-scale computational simulations are conducted in order to investigate the effects of aggregate distribution, aggregate volume fraction, and ITZ thickness and mechanical properties on the overall tensile strength and micro-crack initiation and propagation in concrete. Three-dimensional meso-scale numerical analysis is also carried out for the more realistic prediction of the damage behavior of concrete under tensile loading. For both 2-D and 3-D meso-scale simulations, concrete is considered as a realistic 3-phase composite material (mortar matrix, aggregate, and ITZ), and three different sized aggregate are used. In order to simulate the inelastic and damage behavior of the mortar matrix and the ITZ separately, the coupled plasticity-damage model developed by Cicekli et al. [12] is adopted and modified in this work and implemented in the commercial finite element program Abaqus via the user material subroutine UMAT. For the better prediction of the concrete behavior, the modified isotropic and anisotropic damage models are proposed based on the phenomenological observation that the damaged stiffness varies nonlinearly with the damage density. Moreover, the plastic multiplier and the elasto-plastic tangent stiffness are derived using a semi-implicit numerical algorithm. Detailed numerical algorithms are presented for integrating the coupled plasticity and anisotropic damage constitutive equations for simple implementation into finite element codes. Then, the constitutive model is applied to the meso-scale simulation and prediction of the overall mechanical behavior of concrete composites based on the mechanical properties of their constituents. The presented meso-scale simulations provide valuable insights for relating the microstructure–property relationship in cementitious composites in order to ultimately guide the design of better concrete with enhanced tensile strength, fracture toughness, and ductility. Furthermore, the presented computational framework can be effectively applied to the smaller scale simulation for investigating the effects of fillers (e.g. micro- and nano-fibers, micro- and nano-inclusions) on the overall mechanical behavior of hardened cementitious composites. Existing researches in cementitious material on nanoscopic level have mainly been focused on the effect of the hydration products on the early-age stiffness and strength evolution of cement paste (e.g. [7,34,36]), and the numerical investigation of the effect of the nano-fiber, such as carbon nanotube on the crack initiation and propagation mechanisms and the overall properties of cementitious composites have rarely been made [10]. Such detailed investigations are very difficult to perform through experimental routes and, therefore, the presented computational framework is highly desirable. Special emphasis is placed in this paper on investigating the effects of aggregate shape, distribution, volume fraction, and the ITZ thickness and mechanical properties on the overall tensile behavior of concrete. It is shown in this paper that the aggregate volume fraction and the mechanical properties of the ITZ are the key parameters for controlling the overall macroscopic response and fracture of concrete. Also, it is shown that the conducted two-dimensional simulations of simplified concrete micro-structures provide valuable and valid insights that are comparable to those from more realistic three-dimensional simulations.

The paper is organized as follows: in Section 2, the recently developed coupled plasticity-damage model by Cicekli et al. [12] is recalled and modified to include anisotropic damage evolution and more robust damage evolution laws. The numerical algorithms necessary for implementing the coupled plasticity-damage model in the commercial finite element code Abaqus are presented in Section 3. Section 4 presents the 2-D meso-scale simulations investigating the effects of aggregates shape, distribution, and volume fraction, and the thickness and mechanical properties of the ITZ, and the damage configuration of the 3-D meso-scale model of concrete is addressed in Section 5. Finally, conclusions and future works are emphasized in Section 6.

2. Plastic-damage model for plain concrete

Plasticity, continuum damage mechanics, fracture mechanics, elastic-damage, and combined plasticity and damage mechanics are the common theories that have been used for the description of concrete constitutive behavior. However, the plasticity theory failed to address the degradation of the material stiffness due to micro-cracking, the fracture mechanics approach failed to describe the nucleation of numerous micro-cracks and the growth of the micro-cracks to macro-cracks, the continuum damage mechanics with elasticity also failed to describe the irreversible deformations and the inelastic volumetric expansion in compression. Therefore, since both micro-cracking and irreversible deformations are contributing to the nonlinear response of concrete, a constitutive model should address equally the two physically distinct modes of irreversible changes. In order to address this issue, the coupled plasticity-damage model formulated recently by Cicekli et al. [12] and modified by Abu Al-Rub and Kim [2] for plain concrete is recalled in this section. All the presented constitutive equations were derived based on the laws of thermodynamics and assuming small deformations. In order to predict the plastic behavior of plain concrete, the Lubliner yield criterion [23,28] expressed in the effective (undamaged) configuration is adopted. Moreover, the non-associative plasticity flow rule based on the Drucker–Prager potential and two distinct damage evolution surfaces; tensile and compressive damage surfaces are included in the model.

2.1. Isotropic damage model

The definition of the damage variable φ based on the effective (undamaged) area as proposed by [17] is adopted here. In the effective configuration all types of damages, including both voids and cracks, are considered. The damage density φ is defined by the ratio of the total damaged area to whole cross-sectional area such that:

$$\varphi = \frac{A-\overline{A}}{A} = \frac{A^D}{A} \tag{1}$$

The damage density φ can be varied from 0 to 1. That a damage density equal to 0 means the material is undamaged and 1 means the material is fully damaged.

The relation between the nominal Cauchy stress tensor σ_{ij} and the corresponding effective stress tensor $\overline{\sigma}_{ij}$ for the isotropic damage (i.e. scalar damage variable) can be written as follows:

$$\sigma_{ij} = (1-\varphi)\overline{\sigma}_{ij} \tag{2}$$

Therefore, in the continuum damage mechanics framework, the effective stress means the average micro-level stress acting in the undamaged (intact) material between defects and is defined as the force divided by the undamaged part of the area, while the nominal stress means the macro-level stress and is defined as the force divided by the total area.

However, as argued by Cicekli et al. [12] the damaged stiffness varies nonlinearly with the damage density. Therefore, in order to predict the nonlinear degradation of the damaged stiffness due to the increase of the damage density, a nonlinear relationship between the nominal and the effective stress tensor is assumed, such that:

$$\sigma_{ij} = (1-\varphi)^{\gamma}\overline{\sigma}_{ij} \tag{3}$$

where $\gamma \geq 1$ is a material constant. In the following development $\gamma = 2$ will be assumed such that

$$\sigma_{ij} = (1-\varphi)^2\overline{\sigma}_{ij} \tag{4}$$

In order to derive the transformation relations between the damaged and the hypothetical undamaged states of the material, the strain equivalence hypothesis [55] is adopted in this paper for simplicity and ease in numerical implementation. This hypothesis states that the elastic and plastic strains in both the damaged and the effective configurations due to the applied forces are equivalent. Therefore, the total strain tensor ε_{ij} is set equal to the corresponding effective strain tensor $\overline{\varepsilon}_{ij}$ (i.e. $\varepsilon_{ij} = \overline{\varepsilon}_{ij}$), which can be decomposed into an elastic strain $\varepsilon^e_{ij}\left(=\overline{\varepsilon}^e_{ij}\right)$ and a plastic strain $\varepsilon^p_{ij}\left(=\overline{\varepsilon}^p_{ij}\right)$, such that:

$$\varepsilon_{ij} = \varepsilon^e_{ij} + \varepsilon^p_{ij} = \overline{\varepsilon}^e_{ij} + \overline{\varepsilon}^p_{ij} = \overline{\varepsilon}_{ij} \tag{5}$$

The plastic strain in Eq. (5) incorporates all types of irreversible deformations whether they are due to tensile micro-cracking, breaking of internal bonds during shear loading, and/or compressive consolidation during the collapse of the micro-porous structure of the cement matrix.

Using the generalized Hooke's law, σ_{ij} and $\overline{\sigma}_{ij}$ are given as follows:

$$\sigma_{ij} = E_{ijkl}\varepsilon^e_{kl}, \quad \overline{\sigma}_{ij} = \overline{E}_{ijkl}\varepsilon^e_{kl} \tag{6}$$

For isotropic linear-elastic material, the fourth-order elasticity tensor $\bar{E}_{ijkl}$ for the undamaged material is given by

$$\overline{E}_{ijkl} = 2\overline{G}\delta_{ik}\delta_{jl} + \left(\overline{K}-\frac{2}{3}\overline{G}\right)\delta_{ij}\delta_{kl} \tag{7}$$

where $\overline{G} = \overline{E}/2(1+\overline{\nu})$ and $\overline{K} = \overline{E}/3(1-2\overline{\nu})$ are the effective shear and bulk moduli, respectively, with $\bar{E}$ being the Young's modulus and $\overline{\nu}$ is the Poisson's ratio which are obtained from the stress–strain diagram for the undamaged material.

Applying the hypothesis of the strain equivalence in Eq. (5), the relation between the damaged elasticity tensor E_{ijkl} and $\bar{E}_{ijkl}$ can be expressed by combining Eqs. (4)–(6) as follows:

$$E_{ijkl} = (1-\varphi)^2\overline{E}_{ijkl} \tag{8}$$

The concept of the isotropic damage model applying the hypothesis of the strain equivalence is very simple and has given a lot of inspirations to researchers. One can also use the strain energy equivalence hypothesis [46] to obtain a nonlinear relationship between stiffness and the damage density; however, this will complicate the constitutive models and the numerical implementation. This issue has been discussed thoroughly by Abu Al-Rub and Voyiadjis [3].

Since concrete has a distinct behavior in tension and compression and, therefore, in order to adequately characterize the damage in concrete due to tensile, compressive, and/or cyclic loadings, the Cauchy stress tensor (in the nominal or effective configurations) is decomposed into positive and negative parts using the spectral decomposition technique [20,39,40]. Hereafter, the superscripts "+" and "−" designate, respectively, tensile and compressive entities. Therefore, the nominal stress tensor σ_{ij} and the effective stress tensor $\overline{\sigma}_{ij}$ can be decomposed as follows:

$$\sigma_{ij} = \sigma^+_{ij} + \sigma^-_{ij}, \quad \overline{\sigma}_{ij} = \overline{\sigma}^+_{ij} + \overline{\sigma}^-_{ij} \tag{9}$$

where σ^+_{ij} and $\overline{\sigma}^+_{ij}$ are the tensile parts whereas σ^-_{ij} and $\overline{\sigma}^-_{ij}$ are the compressive parts of the stress tensor.

Using fourth-order tensile and compressive projection tensors P^+_{ijkl} and P^-_{ijkl}, the nominal tensile and compressive stress tensors $\overline{\sigma}^+_{ij}$ and $\overline{\sigma}^-_{ij}$ can be related to $\overline{\sigma}_{ij}$ by

$$\overline{\sigma}^+_{kl} = P^+_{klpq}\overline{\sigma}_{pq}, \quad \overline{\sigma}^-_{kl} = P^-_{klpq}\overline{\sigma}_{pq} \tag{10}$$

where the projection tensors are defined as follows:

$$P^+_{ijpq} = \sum_{k=1}^{3} H\left(\hat{\overline{\sigma}}^{(k)}\right) n_i^{(k)} n_j^{(k)} n_p^{(k)} n_q^{(k)}, \quad P^-_{ijpq} = I_{ijpq} - P^+_{ijpq} \tag{11}$$

where $H\left(\hat{\overline{\sigma}}^{(k)}\right)$ denotes the Heaviside step function computed at kth principal stress $\hat{\overline{\sigma}}^{(k)}$ of $\overline{\sigma}_{ij}$ and $n_i^{(k)}$ is the kth corresponding unit principal directions. In the subsequent development, the superimposed hat designates a principal value.

Based on the decomposition in Eq. (9), the expression in Eq. (4) can be assumed to be valid for both tension and compression independently, such that:

$$\sigma^+_{ij} = \left(1-\varphi^+\right)^2\overline{\sigma}^+_{ij}, \quad \sigma^-_{ij} = (1-\varphi^-)^2\overline{\sigma}^-_{ij} \tag{12}$$

where φ^+ and φ^- are the tensile and compressive damage densities, respectively. Therefore, by substituting Eqs. (12) into Eq. (9), σ_{ij} can be expressed as follows:

$$\sigma_{ij} = \left(1-\varphi^+\right)^2\overline{\sigma}^+_{ij} + (1-\varphi^-)^2\overline{\sigma}^-_{ij} \tag{13}$$

By substituting Eqs. (10) into Eq. (13), one can write the following relation between σ_{ij} and $\overline{\sigma}_{ij}$ in terms of φ^+ and φ^-, such that:

$$\sigma_{ij} = \left[\left(1-\varphi^+\right)^2 P^+_{ijkl} + (1-\varphi^-)^2 P^-_{ijkl}\right]\overline{\sigma}_{kl} \tag{14}$$

2.2. Anisotropic damage

Anisotropic damage is considered in this study for a more reliable representation of concrete damage behavior. Isotropic damage assumes that the strength and stiffness of the concrete material is degraded equally in different directions upon damage evolution which is not realistic for heterogeneous materials like concrete and even for cement paste or mortar phase of the concrete. It is expected that for a heterogeneous material that anisotropic damage is important even under uniaxial loading. Therefore, in order to include damage-induced anisotropy (i.e. different degradation in different directions), the relation between σ_{ij} and $\bar{\sigma}_{ij}$ can be expressed as follows (e.g. [13,32,46]):

$$\sigma_{ij} = M_{ijkl}\bar{\sigma}_{kl} \tag{15}$$

where M_{ijkl} is the fourth-order damage-effect tensor that is used to make the stress tensor symmetrical. There are several definitions for M_{ijkl} [45]; however, the following definition is assumed in this paper, such that:

$$M_{ijkl} = \frac{1}{2}\left[(\delta_{im}-\varphi_{im})\left(\delta_{jm}-\varphi_{jm}\right)\delta_{kl} + \delta_{ij}(\delta_{km}-\varphi_{km})(\delta_{lm}-\varphi_{lm})\right] \tag{16}$$

where δ_{ij} is the Kronecker delta and φ_{ij} is a second-order damage tensor. However, in a future work emphasis will be placed on identifying the underlying micromechanical cracking phenomena that can be used for deriving more physically and microstructurally based anisotropic damage effect tensors as compared to that in Eq. (16). This can be achieved following similar frameworks to that presented, for example, by Pensee et al. [14] and Zhu et al. [54].

By substituting Eq. (15) into Eq. (6), one can express the damaged elasticity tensor E_{ijkl} in terms of the corresponding undamaged elasticity tensor $\bar{E}_{ijkl}$ for the anisotropic damage case and for the strain equivalence hypothesis by the following relation:

$$E_{ijkl} = M_{ijmn}\bar{E}_{mnkl} \tag{17}$$

Based on Eq. (9), the expression in Eq. (15) can be rewritten with decoupled damage evolutions in tension and compression, such that:

$$\sigma_{ij}^{+} = M_{ijkl}^{+}\bar{\sigma}_{kl}^{+}, \quad \sigma_{ij}^{-} = M_{ijkl}^{-}\bar{\sigma}_{kl}^{-} \tag{18}$$

where M_{ijkl}^{+} is the tensile damage-effect tensor and M_{ijkl}^{-} is the corresponding compressive damage effect-tensor which can be expressed using Eq. (16) in a decoupled form as a function of the tensile and compressive damage variables, φ_{ij}^{+} and φ_{ij}^{-}, respectively, as follows:

$$M_{ijkl}^{+} = \frac{1}{2}\left[\left(\delta_{im}-\varphi_{im}^{+}\right)\left(\delta_{jm}-\varphi_{jm}^{+}\right)\delta_{kl} + \delta_{ij}\left(\delta_{km}-\varphi_{km}^{+}\right)\left(\delta_{lm}-\varphi_{lm}^{+}\right)\right] \tag{19}$$

$$M_{ijkl}^{-} = \frac{1}{2}\left[(\delta_{im}-\varphi_{im}^{-})\left(\delta_{jm}-\varphi_{jm}^{-}\right)\delta_{kl} + \delta_{ij}(\delta_{km}-\varphi_{km}^{-})(\delta_{lm}-\varphi_{lm}^{-})\right] \tag{20}$$

Now, by substituting Eq. (18) into Eq. (9), one can express $\bar{\sigma}_{ij}$ as follows:

$$\bar{\sigma}_{ij} = \left(M_{ijkl}^{+}\right)^{-1}\sigma_{kl}^{+} + \left(M_{ijkl}^{-}\right)^{-1}\sigma_{kl}^{-} \tag{21}$$

Similarly, substituting Eqs. (18) into Eq. (9), gives σ_{ij} as follows:

$$\sigma_{ij} = M_{ijkl}^{+}\bar{\sigma}_{kl}^{+} + M_{ijkl}^{-}\bar{\sigma}_{kl}^{-} \tag{22}$$

By substituting Eqs. (10) into Eq. (21) and comparing the result with Eq. (15), the following relation for the damage-effect tensor M_{ijkl} can be obtained, such that:

$$M_{ijpq} = M_{ijkl}^{+}P_{klpq}^{+} + M_{ijkl}^{-}P_{klpq}^{-} \tag{23}$$

Using Eq. (11), the above expression can be rewritten as:

$$M_{ijpq} = \left[M_{ijkl}^{+}-M_{ijkl}^{-}\right]P_{klpq}^{+} + M_{ijpq}^{-} \tag{24}$$

It is also noteworthy that the relation in Eq. (24) enhances a coupling between tensile and compressive damage through the fourth-order projection tensor P_{ijkl}^{+}. Therefore, for isotropic damage Eq. (14) gives the following expression for the fourth-order damage-effect tensor:

$$M_{ijkl} = \left(1-\varphi^{+}\right)^{2}P_{ijkl}^{+} + (1-\varphi^{-})^{2}P_{ijkl}^{-} \tag{25}$$

From the above expression, adopting the decomposition of the scalar damage variable φ into a positive φ^{+} part and a negative φ^{-} part still enhances a damage anisotropy through the spectral decomposition tensors P_{ijkl}^{+} and P_{ijkl}^{-}. However, this anisotropy is weak when compared to the anisotropic damage effect tensor presented in Eq. (24).

2.3. Plasticity yield surface

Concrete materials exhibit plastic (irreversible) deformation upon unloading which implies that an elastic-damage model is not sufficient to model the concrete behavior even under tensile loading conditions. Therefore, an elasto-plastic-damage model should be developed. Thus, a plasticity yield surface and plasticity flow rules need to be developed. Furthermore, since concrete material behaves differently in tension and compression, the yield criterion of Lubliner et al. [28] that accounts for both tension and compression plasticity is adopted in this paper. However, since the stress state in the intact material is the one which drives the plasticity evolution, this yield criterion is expressed in the effective (undamaged) configuration as follows:

$$f = \sqrt{3\bar{J}_2} + \alpha\bar{I}_1 + \beta\left(\varepsilon_{eq}^{+},\varepsilon_{eq}^{-}\right)\mathrm{H}\left(\hat{\bar{\sigma}}_{max}\right)\hat{\bar{\sigma}}_{max} - (1-\alpha)c^{-}\left(\varepsilon_{eq}^{-}\right) \le 0 \tag{26}$$

where $\bar{J}_2 = \bar{s}_{ij}\bar{s}_{ij}/2$ is the second-invariant of the effective deviatoric stress tensor $\bar{s}_{ij} = \bar{\sigma}_{ij} - \bar{\sigma}_{kk}\delta_{ij}/3$, $\bar{I}_1 = \bar{\sigma}_{kk}$ is the first-invariant of the effective Cauchy stress tensor $\bar{\sigma}_{ij}$, $\hat{\bar{\sigma}}_{max}$ is the maximum principal effective stress, $\mathrm{H}\left(\hat{\bar{\sigma}}_{max}\right)$ is the Heaviside step function ($\mathrm{H}=1$ for $\hat{\bar{\sigma}}_{max} > 0$ and $\mathrm{H}=0$ for $\hat{\bar{\sigma}}_{max} < 0$), and the parameters α and β are dimensionless constants which are defined as follows:

$$\alpha = \frac{(f_{b0}/f_0^{-})-1}{2(f_{b0}/f_0^{-})-1}, \quad \beta = (1-\alpha)\frac{c^{-}\left(\varepsilon_{eq}^{-}\right)}{c^{+}\left(\varepsilon_{eq}^{+}\right)} - (1+\alpha) \tag{27}$$

with f_{b0} and f_0^{-} being the initial equi-biaxial and uniaxial compressive yield strengths, respectively. Experimental values for f_{b0}/f_0^{-} lie between 1.10 and 1.16; yielding values for α between 0.08 and 0.12, and 0.12 is used for α constant in this study.

The internal plastic state variables $\varepsilon_{eq}^{+} = \int_0^t \dot{\varepsilon}_{eq}^{+} dt$ and $\varepsilon_{eq}^{-} = \int_0^t \dot{\varepsilon}_{eq}^{-} dt$ are the equivalent plastic strains in tension and compression, respectively, where their rates are defined as follows:

$$\dot{\varepsilon}_{eq}^{+} = r\left(\hat{\bar{\sigma}}_{ij}\right)\dot{\hat{\varepsilon}}_{max}^{p}, \quad \dot{\varepsilon}_{eq}^{-} = -\left(1-r\left(\hat{\bar{\sigma}}_{ij}\right)\right)\dot{\hat{\varepsilon}}_{min}^{p} \tag{28}$$

where $\hat{\varepsilon}_{max}^{p}$ and $\hat{\varepsilon}_{min}^{p}$ are the maximum and minimum principal values of the plastic strain rate $\dot{\varepsilon}_{ij}^{p}$ such that $\hat{\varepsilon}_1^p > \hat{\varepsilon}_2^p > \hat{\varepsilon}_3^p$ with $\hat{\varepsilon}_{max}^{p} = \hat{\varepsilon}_1^p$ and $\hat{\varepsilon}_{min}^{p} = \hat{\varepsilon}_3^p$. Note that the superscript + or − designates a tensile or compressive quantity, $(\hat{\bullet})$ designates the principle value of $(\bullet)$, and the subscripts *eq*, min, and max are not indicial indices. The dimensionless parameter $r\left(\hat{\bar{\sigma}}_{ij}\right)$ is a weighting factor for tension or compression depending on the values of the principal stresses and is defined as follows:

$$r\left(\hat{\bar{\sigma}}_{ij}\right) = \frac{\sum_{k=1}^{3}\left\langle\hat{\bar{\sigma}}_k\right\rangle}{\sum_{k=1}^{3}\left|\hat{\bar{\sigma}}_k\right|} \tag{29}$$

where $\langle\rangle$ is the McAuley bracket presented as $\langle x\rangle = \frac{1}{2}(|x| + x)$. Note that $r\left(\hat{\bar{\sigma}}_{ij}\right) = r\left(\hat{\sigma}_{ij}\right)$. Moreover, depending on the value of $r\left(\hat{\bar{\sigma}}_{ij}\right)$: (a) if the loading is pure uniaxial tension $\hat{\bar{\sigma}}_k \geq 0$, then $r\left(\hat{\bar{\sigma}}_{ij}\right) = 1$, and (b) if the loading is pure uniaxial compression $\hat{\bar{\sigma}}_k \leq 0$, then $r\left(\hat{\bar{\sigma}}_{ij}\right) = 0$.

In the last term of Eq. (26), the isotropic hardening function c^{-}represents the material cohesion in uniaxial compression. Since the concrete behavior in compression is more of a ductile behavior as compared to its corresponding brittle behavior in tension, the evolution of the compressive and tensile isotropic hardening functions c^{-} and c^{+} are defined by the following exponential and linear hardening laws, respectively:

$$c^{-} = f_0^{-} + Q^{-}\left[1-\exp\left(-b^{-}\varepsilon_{eq}^{-}\right)\right], \quad c^{+} = f_0^{+} + h^{+}\varepsilon_{eq}^{+} \tag{30}$$

where f_0^{-} and f_0^{+} are the initial yield stresses in compression and tension (i.e. when nonlinear behavior starts), respectively. The parameters Q^{-}, b^{-}, and h^{+} are material constants, which are obtained in the effective configuration of the uniaxial stress–strain diagram.

For realistic modeling of the volumetric expansion under compression of concrete, a non-associative plasticity flow rule should be used. This can be done by writing the evolution of the plastic strain tensor $\dot{\varepsilon}_{ij}^{p}$, in terms of a plastic potential F^p that is not equal to the plastic yield function f, such that:

$$\dot{\varepsilon}_{ij}^{p} = \dot{\lambda}^{p}\frac{\partial F^{p}}{\partial\bar{\sigma}_{ij}} \tag{31}$$

where $\dot{\lambda}^{p}$ is the plastic multiplier, which can be obtained using the standard plasticity consistency condition, $\dot{f} = 0$, such that:

$$f \leq 0, \quad \dot{\lambda}^{p} \geq 0, \quad \dot{\lambda}^{p} f = 0, \quad \dot{\lambda}^{p}\dot{f} = 0 \tag{32}$$

The plastic potential F^p can be expressed in terms of the Drucker–Prager function as:

$$F^{p} = \sqrt{3\bar{J}_2} + \alpha^{p}\bar{I}_1 \tag{33}$$

where α^p is the dilation material constant. Then the plastic flow direction $\partial F^p / \partial\bar{\sigma}_{ij}$ in Eq. (31) is given by

$$\frac{\partial F^{p}}{\partial\bar{\sigma}_{ij}} = \frac{3}{2}\frac{\bar{s}_{ij}}{\sqrt{3\bar{J}_2}} + \alpha^{p}\delta_{ij} \tag{34}$$

2.4. Tensile and compressive damage surfaces

The following damage growth function which is proposed by Chow and Wang [11] and used by many others (see e.g. [3,4,47,48], and the references quoted therein) is adopted in this study. However, this function is generalized in Cicekli et al. [12] in order to incorporate both tensile and compressive damage separately, such that:

$$g^{\pm} = \sqrt{\frac{1}{2}Y_{ij}^{\pm}L_{ijkl}^{\pm}Y_{kl}^{\pm}} - K^{\pm}\left(\varphi_{eq}^{\pm}\right) \leq 0 \tag{35}$$

where $K^{\pm}$ is the tensile or compressive damage isotropic hardening function such that $K^{\pm} = K_0^{\pm}$ when there is no damage, where $K_0^{\pm}$ is the tensile or compressive initial damage parameter (i.e. damage threshold), and $L_{ijkl}^{\pm}$ is a fourth-order symmetric tensor and is presented in matrix form as follows:

$$L_{ijkl}^{\mp} = \begin{bmatrix} 1 & \mu^{\pm} & \mu^{\pm} & 0 & 0 & 0 \\ \mu^{\pm} & 1 & \mu^{\pm} & 0 & 0 & 0 \\ \mu^{\pm} & \mu^{\pm} & 1 & 0 & 0 & 0 \\ 0 & 0 & 0 & 2\left(1-\mu^{\pm}\right) & 0 & 0 \\ 0 & 0 & 0 & 0 & 2\left(1-\mu^{\pm}\right) & 0 \\ 0 & 0 & 0 & 0 & 0 & 2\left(1-\mu^{\pm}\right) \end{bmatrix} \tag{36}$$

where $\mu^{\pm}$ is a material constant satisfying $-1/2 \leq \mu^{\pm} \leq 1$. However, in what follows, $L_{ijkl}^{\pm}$ is taken as the fourth-order identity tensor I_{ijkl} in order to simplify the anisotropic damage formulation.

The damage driving force $Y_{ij}^{\pm}$ is interpreted as the energy release rate according to the notion of fracture mechanics as argued by Abu Al-Rub and Voyiadjis [3], where the following expression is proposed:

$$Y_{rs}^{\pm} = -\frac{1}{2}\bar{E}_{ijab}^{-1}\bar{\sigma}_{ab}\frac{\partial M_{ijpq}}{\partial\varphi_{rs}^{\pm}}\bar{\sigma}_{pq} \tag{37}$$

The rate of the equivalent damage $\dot{\varphi}_{eq}^{\pm}$ (i.e. rate of damage accumulation) is defined as:

$$\dot{\varphi}_{eq}^{\pm} = \sqrt{\dot{\varphi}_{ij}^{\pm}\dot{\varphi}_{ij}^{\pm}} \quad \text{with} \quad \varphi_{eq}^{\pm} = \int_0^t \dot{\varphi}_{eq}^{\pm} dt \tag{38}$$

where the evolution equation for $\dot{\varphi}_{ij}^{\pm}$ is defined by:

$$\dot{\varphi}_{ij}^{\pm} = \dot{\lambda}_d^{\pm}\frac{\partial g^{\pm}}{\partial Y_{ij}^{\pm}} \tag{39}$$

where $\dot{\lambda}_d^{\pm}$ is the damage multiplier such that one can easily show from Eqs. (35)–(39) that $\dot{\lambda}_d^{\pm} = \dot{\varphi}^{\pm}$. This multiplier can be obtained from the following damage consistency conditions:

$$g^{\pm} \leq 0, \quad \dot{\lambda}_d^{\pm} g^{\pm} = 0, \quad \text{and} \quad \dot{g}^{\pm}\begin{Bmatrix} <0 \Rightarrow \dot{\lambda}_d^{\pm} = 0 \\ = 0 \Rightarrow \dot{\lambda}_d^{\pm} = 0 \\ = 0 \Rightarrow \dot{\lambda}_d^{\pm} > 0 \end{Bmatrix} \Leftrightarrow \begin{Bmatrix} \text{effective (undamaged state)} \\ \text{damage initiation} \\ \text{damage growth} \end{Bmatrix} \tag{40}$$

The following power tensile and compressive damage evolution laws are proposed in order to improve the capability of the damage model for the prediction of the concrete behavior and to compare it to the exponential damage low which is widely used in the literature, such that:

$$\varphi_{eq}^{+} = B^{+}\left(\frac{K_0^{+}}{K^{+}}\right)\left(\frac{K^{+}}{K_0^{+}} - 1\right)^{q^{+}} \tag{41}$$

$$\varphi_{eq}^{-} = B^{-}\left(\frac{K^{-}}{K_0^{-}} - 1\right)^{q^{-}} \tag{42}$$

where $B^{\pm}$ and $q^{\pm}$ are material constants. The expense of this proposition is that one needs to identify more material constant from experimental data as compared to the exponential damage laws. However, it will be shown in the analysis section that even setting $q^{\pm}=1$ gives better predictions than the exponential damage laws.

Similarly, for the power damage laws, one can obtain the evolution of the damage isotropic hardening functions $\dot{K}^{+}$ and $\dot{K}^{-}$ by taking the time derivative of Eqs. (41) and (42) as follows:

$$\dot{K}^{+}=\frac{K^{+}}{B^{+}\left(q^{+}K_0^{+}-1+\frac{K_0^{+}}{K^{+}}\right)}\left[\frac{K^{+}}{K_0^{+}}-1\right]^{1-q^{+}}\dot{\varphi}_{eq}^{+} \tag{43}$$

$$\dot{K}^{-}=\frac{K_0^{-}}{B^{-}q^{-}}\left[\frac{K^{-}}{K_0^{-}}-1\right]^{1-q^{-}}\dot{\varphi}_{eq}^{-} \tag{44}$$

It is noted that the tensile and compressive exponential and power damage evolution laws in Eqs. (41) and (42) obey the fundamental principle that the damage is not initiated until the damage hardening function $K^{\pm}$ is greater than the damage threshold $K_0^{\pm}$.

3. Numerical implementation

In this section, the time descretization and numerical integration procedures for the current elasto-plastic-damage model are presented. The evolutions of the plastic and damage internal state variables can be obtained if the Lagrangian multipliers $\dot{\lambda}^{p}$ and $\dot{\lambda}_d^{\pm}$ are computed. Therefore, the plasticity and damage consistency conditions, Eqs. (32) and (40), are used for computing both $\dot{\lambda}^{p}$ and $\dot{\lambda}_d^{\pm}$. This is shown in the subsequent developments. Then, at the beginning of the step, by applying the given strain increment $\Delta\varepsilon_{ij}=\varepsilon_{ij}^{(n+1)}-\varepsilon_{ij}^{(n)}$ and knowing the values of the stress and internal variables from the previous step, $(\bullet)^{(n)}$, the updated values at the end of the step, $(\bullet)^{(n+1)}$, are obtained.

The implemented integration scheme is divided into two sequential steps, corresponding to the plastic and damage parts of the model. In the plastic part, the plastic strain ε_{ij}^{p} and the effective stress $\overline{\sigma}_{ij}$ at the end of the step are determined by using the classical radial return mapping algorithm (Simo and Hughes in [38]), such that one can write from Eqs. (6), (5), and (31) the following algorithmic step:

$$\overline{\sigma}_{ij}^{(n+1)}=\overline{\sigma}_{ij}^{tr}-\overline{E}_{ijkl}\varepsilon_{kl}^{p}=\overline{\sigma}_{ij}^{tr}-\lambda^{p}\overline{E}_{ijkl}\frac{\partial F^{p(n+1)}}{\partial\overline{\sigma}_{kl}} \tag{45}$$

where $\overline{\sigma}_{ij}^{tr}=\overline{\sigma}_{ij}^{(n)}+\overline{E}_{ijkl}\varepsilon_{kl}$ is the trial stress tensor, which is easily evaluated from the given strain increment. Also, substituting Eqs. (7) and (34) into Eq. (45), the above equation can be rewritten as follows:

$$\overline{\sigma}_{ij}^{(n+1)}=\overline{\sigma}_{ij}^{tr}-\lambda^{p}\left[\sqrt{6}\,\overline{G}\frac{\overline{s}_{ij}^{(n+1)}}{\left\|\overline{s}_{ij}^{(n+1)}\right\|}+3\overline{K}\alpha^{p}\delta_{ij}\right] \tag{46}$$

where $\|\overline{s}_{ij}\|=\sqrt{\overline{s}_{ij}\overline{s}_{ij}}$ and $\overline{s}_{ij}$ is the deviatoric component of the effective stress tensor $\overline{\sigma}_{ij}$. If the trial stress is inside the yield surface, i.e. $f\left(\overline{\sigma}_{ij}^{tr},c_c^{(n)}\right)\le 0$, the step is elastic and one sets $\lambda^{p}=0$, $\overline{\sigma}_{ij}^{tr}=\overline{\sigma}_{ij}^{(n+1)}$, $\varepsilon_{ij}^{p(n+1)}=\varepsilon_{ij}^{p(n)}$, $c^{\pm(n+1)}=c^{\pm(n)}$. However, if the trial stress is outside the yield surface, then $\overline{\sigma}_{ij}^{(n+1)}$, $\varepsilon_{ij}^{p(n+1)}$, and $c^{\pm(n+1)}$ are determined by computing λ^{p} as shown next.

In the damage part, the nominal stress σ_{ij} at the end of the step is obtained from Eq. (15) by knowing the damage variables $\varphi_{ij}^{\pm}$, which can be calculated once $\Delta\lambda_d^{\pm}$ are computed from the damage consistency conditions in Eq. (40) as will be shown in the subsequent developments.

3.1. Computation of the plastic multiplier

In this section, the plastic consistency condition in Eq. (32) is satisfied at the end of the loading step in order to calculate the plastic multiplier $\Delta\lambda^{p}$, such that one can write from Eq. (26):

$$f^{(n+1)}=\sqrt{\frac{3}{2}}\left\|\overline{s}_{ij}^{(n+1)}\right\|+\alpha\overline{I}_1^{(n+1)}-\beta^{(n+1)}H\left(\hat{\overline{\sigma}}_{max}^{(n+1)}\right)\hat{\overline{\sigma}}_{max}^{(n+1)}-(1-\alpha)c^{-(n+1)}=0 \tag{47}$$

However, in order to return radially to the yield surface, one needs to assume (Simo and Hughes in [41]):

$$\frac{\overline{s}_{ij}^{(n+1)}}{\left\|\overline{s}_{ij}^{(n+1)}\right\|}=\frac{\overline{s}_{ij}^{tr}}{\left\|\overline{s}_{ij}^{tr}\right\|} \tag{48}$$

where $\overline{s}_{ij}^{tr}=\overline{\sigma}_{ij}^{tr}-\frac{1}{3}\overline{\sigma}_{kk}^{tr}\delta_{ij}$. Therefore, at step $n+1$, one can write from Eq. (46) the following expressions for the deviatoric stress and the corresponding volumetric stress, respectively:

$$\overline{s}_{ij}^{(n+1)}=\overline{s}_{ij}^{tr}-\lambda^{p}\sqrt{6}\,\overline{G}\frac{\overline{s}^{ijtr}}{\|\overline{s}_{ij}^{tr}\|} \tag{49}$$

$$\overline{I}_1^{(n+1)}=\overline{I}_1^{tr}-9\lambda^{p}\overline{K}\alpha_p \tag{50}$$

Multiplying both sides of Eq. (49) by $\overline{s}_{ij}^{tr}$ and applying the assumption of Eq. (48), the deviatoric stress in Eq. (49) can be rewritten as follows:

$$\left\|\overline{s}_{ij}^{(n+1)}\right\|=\left\|\overline{s}_{ij}^{tr}\right\|-\sqrt{6}\,\overline{G}\lambda^{p} \tag{51}$$

Now, since the yield function includes the principal stress, $\hat{\overline{\sigma}}_{max}^{(n+1)}$, one needs an expression for $\hat{\overline{\sigma}}_{max}^{(n+1)}$ similar to that obtained in Eq. (49). One can express $\overline{\sigma}_{ij}^{(n+1)}$ in terms of the principal stresses $\hat{\overline{\sigma}}_{ij}^{(n+1)}$ as follows:

$$\overline{\sigma}_{ij}^{(n+1)}=l_{ir}\hat{\overline{\sigma}}_{rs}^{(n+1)}l_{js} \tag{52}$$

where $l_{ij}=\left[n_i^{(1)}\quad n_i^{(2)}\quad n_i^{(3)}\right]^{T}$ is a second-order tensor that contains the principal directions of $\overline{\sigma}_{ij}$, where $n_i^{(1)}$, $n_i^{(2)}$, and $n_i^{(3)}$ are the eigenvectors that correspond to $\hat{\overline{\sigma}}^{(1)}=\hat{\overline{\sigma}}_{max}$, $\hat{\overline{\sigma}}^{(2)}$, and $\hat{\overline{\sigma}}^{(3)}=\hat{\overline{\sigma}}_{min}$, respectively, and $[]^{T}$ designates the transpose. Also, one can write from Eq. (33) $F^{p}\left(\overline{\sigma}_{ij}^{(n+1)}\right)=F^{p}\left(\hat{\overline{\sigma}}_{ij}^{(n+1)}\right)$. As a result, one can write the following expressions from Eq. (31) in terms of the principal values as follows:

$$\frac{\partial F^{p(n+1)}}{\partial\overline{\sigma}_{ij}}=l_{ir}\frac{\partial F^{p}}{\partial\hat{\overline{\sigma}}_{rs}^{(n+1)}}l_{js} \tag{53}$$

By substituting Eqs. (52), and (53) into Eq. (45) along with using Eq. (7), one can write the following expression:

$$\hat{\overline{\sigma}}_{ij}^{(n+1)}=\hat{\overline{\sigma}}_{ij}^{tr}-\Delta\lambda^{p}\left[2\overline{G}\frac{\partial F}{\partial\hat{\overline{\sigma}}_{ij}^{(n+1)}}+3\left(\overline{K}-\frac{2}{3}\overline{G}\right)\alpha_p\delta_{ij}\right] \tag{54}$$

where the derivative of the plastic potential function with respect to the principal stresses is given as follows:

$$\frac{\partial F}{\partial\hat{\overline{\sigma}}_{ij}^{(n+1)}}=\sqrt{\frac{3}{2}}\frac{\hat{\overline{s}}_{ij}^{(n+1)}}{\left\|\hat{\overline{s}}_{ij}^{(n+1)}\right\|}+\alpha_p\delta_{ij} \tag{55}$$

However, using Eq. (48), one can rewrite the above expression as follow:

$$\frac{\partial F}{\partial \hat{\bar{\sigma}}_{ij}^{(n+1)}} = \sqrt{\frac{3}{2}}\frac{\hat{\bar{\sigma}}_{ij}^{tr}}{||\hat{\bar{s}}_{ij}^{tr}||} + \left(\alpha_p - \frac{1}{\sqrt{6}}\frac{\bar{I}_1^{tr}}{||\hat{\bar{s}}_{ij}^{tr}||}\right)\delta_{ij} \tag{56}$$

where $\bar{I}_1^{tr} = \hat{\bar{I}}_1^{tr}$ and $||\bar{s}_{ij}^{tr}|| = ||\hat{\bar{s}}_{ij}^{tr}||$. By substituting Eq. (56) into Eq. (54), one can obtain the corrected principal stress as follows:

$$\hat{\bar{\sigma}}_{ij}^{(n+1)} = \hat{\bar{\sigma}}_{ij}^{tr} - \Delta\lambda^p\left[\sqrt{6}\,\bar{G}\,\frac{\hat{\bar{\sigma}}_{ij}^{tr}}{||\bar{s}_{ij}^{tr}||} + \left(3\bar{K}\alpha_p - \sqrt{\frac{2}{3}}\,\bar{G}\frac{\bar{I}_1^{tr}}{||\bar{s}_{ij}^{tr}||}\right)\delta_{ij}\right] \tag{57}$$

Therefore, from Eq. (57), one can easily write an expression for the corrected maximum principal stress $\hat{\bar{\sigma}}_{max}^{(n+1)}$ as follows:

$$\hat{\bar{\sigma}}_{max}^{(n+1)} = \hat{\bar{\sigma}}_{max}^{tr} - \Delta\lambda^p\left[\sqrt{6}\,\bar{G}\frac{\hat{\bar{\sigma}}_{max}^{tr}}{||\bar{s}_{ij}^{tr}||} + \left(3\bar{K}\alpha_p - \sqrt{\frac{2}{3}}\,\bar{G}\frac{\bar{I}_1^{tr}}{||\bar{s}_{ij}^{tr}||}\right)\right] \tag{58}$$

In Eq. (47), the term $\beta^{(n+1)}H\left(\hat{\bar{\sigma}}_{max}^{(n+1)}\right)\hat{\bar{\sigma}}_{max}^{(n+1)}$ can be expressed as follows:

$$\beta^{(n+1)}H\left(\hat{\bar{\sigma}}_{max}^{(n+1)}\right)\hat{\bar{\sigma}}_{max}^{(n+1)} = \beta^{(n)}H\left(\hat{\bar{\sigma}}_{max}^{(n+1)}\right)\hat{\bar{\sigma}}_{max}^{(n+1)} + \Delta\beta H\left(\hat{\bar{\sigma}}_{max}^{(n+1)}\right)\hat{\bar{\sigma}}_{max}^{(n+1)} \tag{59}$$

where the dimensionless constant β is already defined in Eq. (27) and its increment can be expressed as follows:

$$\begin{aligned}\Delta\beta &= \frac{(1-\alpha)}{c^+}\Delta c^- - \frac{(1-\alpha)c^-}{(c^+)^2}\Delta c^+ \\ &= \Delta\lambda^p\left[\frac{(1-r)}{c^+}\frac{\partial f}{\partial \varepsilon_{eq}^-}\frac{\partial F^p}{\partial \hat{\bar{\sigma}}_{min}} + \frac{r}{\left\langle\hat{\bar{\sigma}}_{max}\right\rangle}\frac{\partial f}{\partial \varepsilon_{eq}^+}\frac{\partial F^p}{\partial \hat{\bar{\sigma}}_{max}}\right]\end{aligned} \tag{60}$$

where

$$\frac{\partial f}{\partial \varepsilon_{eq}^+} = -\left\langle\hat{\bar{\sigma}}_{max}\right\rangle\frac{c^-(1-\alpha)h^+}{(c^+)^2} \tag{61}$$

$$\frac{\partial f}{\partial \varepsilon_{eq}^-} = -(1-\alpha)\left[Q^-b^-\exp\left(-b^-\varepsilon_{eq}^-\right)\right] \tag{62}$$

and the increment of the tensile and compressive isotropic hardening functions is expressed as follows from the Eqs. (30):

$$\Delta c^+ = \frac{\partial c^+}{\partial \varepsilon_{eq}^+}\Delta\varepsilon_{eq}^+ = rh^+\Delta\lambda^p\frac{\partial F^p}{\partial \hat{\bar{\sigma}}_{max}} \tag{63}$$

$$\Delta c^- = \frac{\partial c^-}{\partial \varepsilon_{eq}^-}\Delta\varepsilon_{eq}^- = -(1-r)\left[Q^-b^-\exp\left(-b^-\varepsilon_{eq}^-\right)\right]\Delta\lambda^p\frac{\partial F^p}{\partial \hat{\bar{\sigma}}_{min}} \tag{64}$$

By substituting Eqs. (58) and (60) into Eq. (59), one obtains:

$$\begin{aligned}\beta^{(n+1)}H\left(\hat{\bar{\sigma}}_{max}^{(n+1)}\right)\hat{\bar{\sigma}}_{max}^{(n+1)} &= \beta^{(n)}H\left(\hat{\bar{\sigma}}_{max}^{tr}\right)\hat{\bar{\sigma}}_{max}^{tr} - \beta^{(n)}H\left(\hat{\bar{\sigma}}_{max}^{tr}\right)Z\Delta\lambda^p \\ &\quad + r\Delta\lambda^p\frac{\partial f}{\partial \varepsilon_{eq}^{+\,tr}}\frac{\partial F^p}{\partial \hat{\bar{\sigma}}_{max}^{tr}}\end{aligned} \tag{65}$$

where

$$Z = \sqrt{6}\,\bar{G}\frac{\hat{\bar{\sigma}}_{max}^{tr}}{||\bar{s}_{ij}^{tr}||} + 3\bar{K}\alpha_p - \sqrt{\frac{2}{3}}\,\bar{G}\frac{\bar{I}_1^{tr}}{||\bar{s}_{ij}^{tr}||} \tag{66}$$

Moreover, the fourth term of Eq. (47) can also be rewritten as follows:

$$\begin{aligned}(1-\alpha)c^{-(n+1)} &= (1-\alpha)c^{-(n)} + (1-\alpha)\Delta c^- \\ &= (1-\alpha)c^{-(n)} + (1-r)\frac{\partial f}{\partial \varepsilon_{eq}^-}\Delta\lambda^p\frac{\partial F^p}{\partial \hat{\bar{\sigma}}_{min}}\end{aligned} \tag{67}$$

Finally, by substituting Eqs. (50), (51), (65), and (67) into Eq. (47), and making few algebraic manipulations, the plastic multiplier $\Delta\lambda^p$ can then be expressed as follows:

$$\Delta\lambda^p = \frac{f^{tr}}{H} \tag{68}$$

where f^{tr} and H are given as:

$$f^{tr} = \sqrt{\frac{3}{2}}||\bar{s}_{ij}^{tr}|| + \alpha\bar{I}_1^{tr} + \beta^{(n)}H\left(\hat{\bar{\sigma}}_{max}^{tr}\right)\hat{\bar{\sigma}}_{max}^{tr} - (1-\alpha)c^{-(n)} \tag{69}$$

$$H = 3\bar{G} + 9\bar{K}\alpha_p\alpha + \beta^{(n)}H\left(\hat{\bar{\sigma}}_{max}^{tr}\right)Z + (1-r)\frac{\partial f}{\partial \varepsilon_{eq}^{-tr}}\frac{\partial F^p}{\partial \hat{\bar{\sigma}}_{min}^{tr}} - r\frac{\partial f}{\partial \varepsilon_{eq}^{+tr}}\frac{\partial F^p}{\partial \hat{\bar{\sigma}}_{max}^{tr}} \tag{70}$$

3.2. The elasto-plastic tangent stiffness in the effective configuration

In order to accelerate convergence, the elasto-plastic tangent stiffness is needed. From Eqs. (26) and (32), one can express the plasticity consistency condition in the effective configuration (i.e. $\dot{f}$) as follows:

$$\Delta f = \frac{\partial f}{\partial \bar{\sigma}_{ij}}\Delta\bar{\sigma}_{ij} + \frac{\partial f}{\partial \hat{\bar{\sigma}}_{max}}\hat{\bar{\sigma}}_{max} + \frac{\partial f}{\partial \varepsilon_{eq}^+}\Delta\varepsilon_{eq}^+ + \frac{\partial f}{\partial \varepsilon_{eq}^-}\Delta\varepsilon_{eq}^- = 0 \tag{71}$$

One can express $\Delta\bar{\sigma}_{ij}$ and $\Delta\hat{\bar{\sigma}}_{max}$ from Eqs. (45) and (58), respectively, as follows:

$$\Delta\bar{\sigma}_{ij} = 2\bar{G}\Delta\bar{\varepsilon}_{ij} + \left(\bar{K} - \frac{2}{3}\bar{G}\right)\Delta\bar{\varepsilon}_{kk}\delta_{ij} - \Delta\lambda^p\left[\sqrt{6}\,\bar{G}\,\frac{\bar{s}_{ij}^{tr}}{||\bar{s}_{ij}^{tr}||} + 3\bar{K}\alpha^p\delta_{ij}\right] \tag{72}$$

$$\begin{aligned}\Delta\hat{\bar{\sigma}}_{max} &= 2\bar{G}n_i^{(1)}\Delta\bar{\varepsilon}_{ij}n_j^{(1)} + \left(\bar{K} - \frac{2}{3}\bar{G}\right)\Delta\bar{\varepsilon}_{kk} \\ &\quad - \Delta\lambda^p\left[\sqrt{6}\,\bar{G}\frac{\hat{\bar{\sigma}}_{max}^{tr}}{||\bar{s}_{ij}^{tr}||} + \left(3\bar{K}\alpha_p - \sqrt{\frac{2}{3}}\,\bar{G}\frac{\bar{I}_1^{tr}}{||\bar{s}_{ij}^{tr}||}\right)\right]\end{aligned} \tag{73}$$

where $\Delta\bar{\varepsilon}_{ij}$ is the total strain increment and $n_i^{(1)}$ is the eigenvector that corresponds to $\hat{\bar{\sigma}}_{max}$.

By substituting Eqs. (72), (73), and the increments $\Delta\varepsilon_{eq}^+$ and $\Delta\varepsilon_{eq}^-$ from Eqs. (28) into Eq. (71) and making few algebraic manipulations, one can get the expression of the plastic multiplier $\Delta\lambda^p$ as a function of the total strain increment $\Delta\bar{\varepsilon}_{ij}$ as follows:

$$\Delta\lambda^p = \frac{1}{H}\left\{\frac{\partial f}{\partial \bar{\sigma}_{ij}}E_{ijkl} + 2\bar{G}\frac{\partial f}{\partial \hat{\bar{\sigma}}_{max}}n_k^{(1)}n_l^{(1)} + \left(\bar{K} - \frac{2}{3}\bar{G}\right)\frac{\partial f}{\partial \hat{\bar{\sigma}}_{max}}\delta_{kl}\right\}\Delta\bar{\varepsilon}_{kl} \tag{74}$$

where H is already given in Eq. (70). Then, by substituting Eq. (74) into Eq. (72), the stress rate $\Delta\bar{\sigma}_{ij}$ can be rewritten as a function of the rate of the total strain $\Delta\bar{\varepsilon}_{ij}$ as follows:

$$\Delta\bar{\sigma}_{ij} = \bar{D}_{ijkl}\Delta\bar{\varepsilon}_{kl} \tag{75}$$

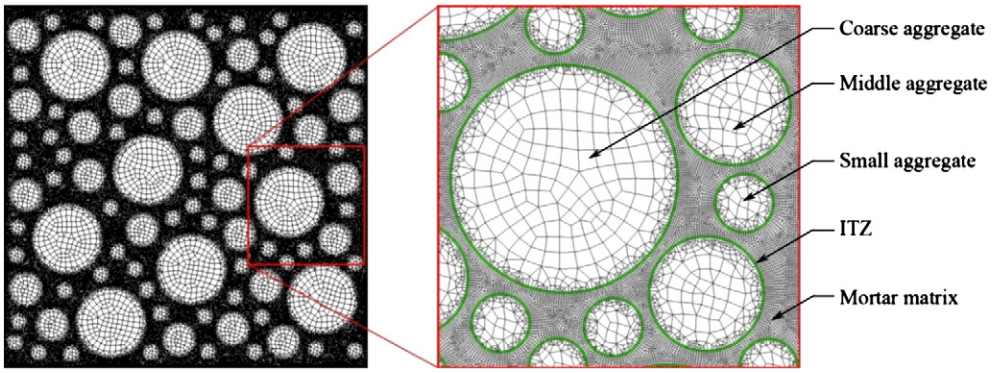

Fig. 1. The 2-D meso-scale concrete analysis model of 60% of aggregate volume fraction.

where the fourth-order tensor $\overline{D}_{ijkl}$ represents the elasto-plastic tangent stiffness in the effective (undamaged) configuration and is expressed as follows:

$$\overline{D}_{ijkl} = \overline{E}_{ijkl} - \frac{1}{H}\left\{\overline{E}_{mnkl}\frac{\partial f}{\partial \overline{\sigma}_{mn}} + \frac{\partial f}{\partial \hat{\overline{\sigma}}}_{max}\left[2\overline{G}n_k^{(1)}n_l^{(1)} + \left(\overline{K} - \frac{2}{3}\overline{G}\right)\right]\delta_{kl}\right\}\overline{E}_{ijpq}\frac{\partial F^p}{\partial \overline{\sigma}_{pq}} \tag{76}$$

The above equation retains $\overline{D}_{ijkl} = \overline{E}_{ijkl}$ if the material is under elastic deformation or there is no plastic flow.

3.3. Computation of the tensile and compressive damage multipliers

In the following, the damage multipliers, $\dot{\lambda}_d^{\pm}$, are obtained using the damage consistency conditions in Eq. (40). The incremental expression for the damage consistency condition can be written as:

$$g^{\pm(n+1)} = g^{\pm(n)} + \Delta g^{\pm} = 0 \tag{77}$$

where $g^{\pm}$ is the damage surface function given in Eq. (35) and $\Delta g^{\pm}$ is the increment of the damage function which is expressed by:

$$\Delta g^{\pm} = \frac{\partial g^{\pm}}{\partial Y_{ij}^{\pm}}\Delta Y_{ij}^{\pm} + \frac{\partial g^{\pm}}{\partial K^{\pm}}\Delta K^{\pm} \tag{78}$$

However, since $Y_{ij}^{\pm}$ is a function of $\sigma_{ij}^{\pm}$ and $\varphi_{ij}^{\pm}$ one can write the following:

$$\Delta Y_{ij}^{\pm} = \frac{\partial Y_{ij}^{\pm}}{\partial \sigma_{kl}^{\pm}}\Delta\sigma_{kl}^{\pm} + \frac{\partial Y_{ij}^{\pm}}{\partial \varphi_{kl}^{\pm}}\Delta\varphi_{kl}^{\pm} \tag{79}$$

where $\Delta\varphi_{kl}^{\pm}$ is obtained from Eqs. (39), such that:

$$\Delta\varphi_{kl}^{\pm} = \Delta\lambda_d^{\pm}\frac{\partial g^{\pm}}{\partial Y_{kl}^{\pm}} \tag{80}$$

and $\Delta\sigma_{kl}^{\pm}$ can be obtained from Eqs. (18) as follows:

$$\Delta\sigma_{kl}^{\pm} = \frac{\partial M_{klrs}^{\pm}}{\partial \varphi_{mn}^{\pm}}\Delta\varphi_{mn}^{\pm}\overline{\sigma}_{rs}^{\pm} + M_{klrs}^{\pm}\Delta\overline{\sigma}_{rs}^{\pm} \tag{81}$$

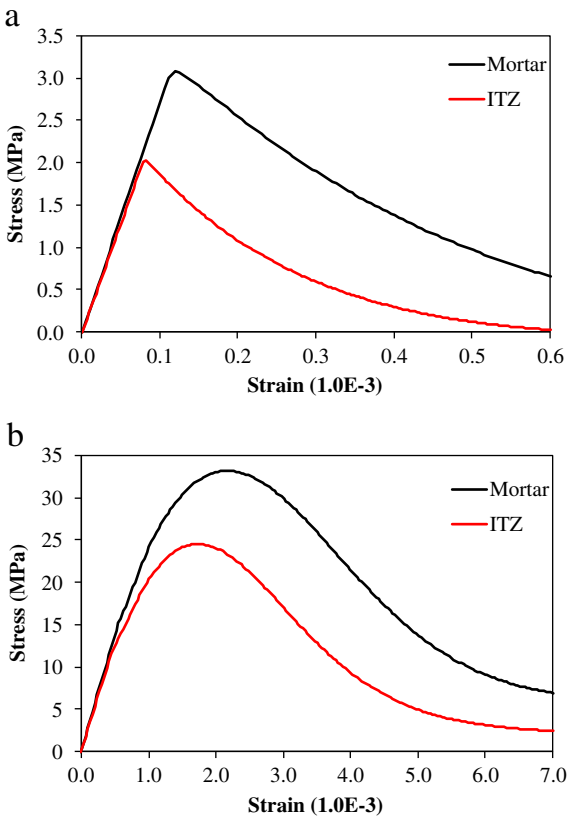

Fig. 2. Stress–strain relation of the mortar and the ITZ. (a) Tensile, (b) compressive.

By substituting Eqs. (79)–(81) into Eq. (78) and noticing that $\dot{\lambda}^{\pm} = \dot{\varphi}_{eq}^{\pm} = \sqrt{\dot{\varphi}_{ij}^{\pm}\dot{\varphi}_{ij}^{\pm}}$, one can obtain the following relation:

$$\Delta g^{\pm} = \frac{\partial g^{\pm}}{\partial Y_{ij}^{\pm}}\frac{\partial Y_{ij}^{\pm}}{\partial \sigma_{kl}^{\pm}}\frac{\partial M_{klrs}^{\pm}}{\partial \varphi_{mn}^{\pm}}\overline{\sigma}_{rs}^{\pm}\frac{\partial g^{\pm}}{\partial Y_{mn}^{\pm}}\Delta\lambda_d^{\pm} + \frac{\partial g^{\pm}}{\partial Y_{ij}^{\pm}}\frac{\partial Y_{ij}^{\pm}}{\partial \sigma_{kl}^{\pm}}M_{klrs}^{\pm}\Delta\overline{\sigma}_{rs}^{\pm} + \frac{\partial g^{\pm}}{\partial Y_{ij}^{\pm}}\frac{\partial Y_{ij}^{\pm}}{\partial \varphi_{kl}^{\pm}}\frac{\partial g^{\pm}}{\partial Y_{kl}^{\pm}}\Delta\lambda_d^{\pm} + \frac{\partial g^{\pm}}{\partial K^{\pm}}\frac{\partial K^{\pm}}{\partial \varphi_{eq}^{\pm}}\Delta\lambda_d^{\pm} \tag{82}$$

Table 1
Material properties used in the analysis.

	Elastic constants		Tensile material constants					Yield criteria		Compressive material constants					
	$\bar{E}$ (MPa)	ν	f_0^+ (MPa)	K_0^+ (MPa)	h^+ (MPa)	B^+	q^+	α	α_p	f_0^- (MPa)	Q^- (MPa)	b^-	K_0^- (MPa)	B^-	q^-
Mortar	26,000	0.20	3.0	3.0	10,000	1.30	1.10	0.12	0.20	15.0	80.0	820.0	20.0	0.15	1.40
ITZ	25,000	0.16	2.0	2.0	10,000	1.40	1.05			12.0	50.0	820.0	16.0	0.20	1.60

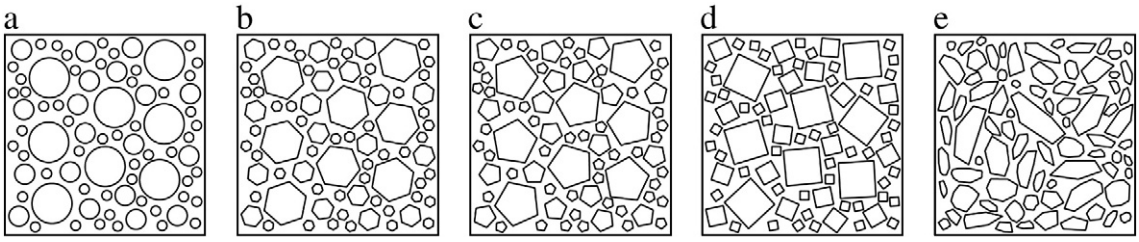

Fig. 3. Aggregate shape sensitivity analysis micro-structures. (a) Circular, (b) hexagonal, (c) pentagonal, (d) tetragonal, and (e) arbitrary polygonal RVEs.

Substituting Eq. (82) into Eq. (77), one obtains $\Delta\lambda_d^{\pm}$ by the following relation:

$$\Delta\lambda_d^{\pm} = \frac{g^{\pm tr}}{H_d^{\pm}} \tag{83}$$

where $g^{\pm tr}$ is the trial value of the damage function, $H_d^{\pm}$ is the tensile or compressive damage modulus and is given as follows:

$$H_d^{\pm} = \frac{\partial g^{\pm}}{\partial Y_{ij}^{\pm}} \frac{\partial Y_{ij}^{\pm}}{\partial \sigma_{kl}^{\pm}} \frac{\partial M_{klrs}^{\pm}}{\partial \varphi_{mn}^{\pm}} \overline{\sigma}_{rs}^{\pm} \frac{\partial g^{\pm}}{\partial Y_{mn}^{\pm}} + \frac{\partial g^{\pm}}{\partial Y_{ij}^{\pm}} \frac{\partial Y_{ij}^{\pm}}{\partial \varphi_{kl}^{\pm}} \frac{\partial g^{\pm}}{\partial Y_{kl}^{\pm}} + \frac{\partial g^{\pm}}{\partial K^{\pm}} \frac{\partial K^{\pm}}{\partial \varphi_{eq}^{\pm}} \tag{84}$$

where

$$\frac{\partial K^{\pm}}{\partial \varphi_{eq}^{\pm}} = \frac{K_0^{\pm}}{B^{\pm} q^{\pm}} \left(\frac{B}{\varphi_{eq}^{\pm}} \right)^{\frac{q^{\pm}-1}{q^{\pm}}} \tag{85}$$

and $\partial g/\partial K^{\pm} = -1$ and the expressions for $\partial g/\partial Y_{ij}$, $\partial Y_{ij}/\partial \sigma_{kl}$, $\partial M_{klrs}^{-1}/\partial \varphi_{mn}$, and $\partial Y_{ij}/\partial \varphi_{kl}$ can be found in Abu Al-Rub and Voyiadjis [3].

4. 2-D meso-scale simulations

The effect of the change of plain concrete properties, such as aggregate shape, size, distribution, and volume fraction, the thickness of the interfacial transmission zone (ITZ), and the strength of the ITZ and mortar matrix on the tensile behavior of concrete is investigated here with 2-D meso-scale numerical simulations. The current elasto-plastic-damage model is implemented in the well-known finite element code Abaqus via the user material subroutine UMAT and is used in conducting the following meso-scale simulations. A 4-node bilinear plane stress quadrilateral element (CPS4R) is used for all models. Fig. 1 shows the representative volume element (RVE) of size 100 mm × 100 mm, which is found to be representative of the statistical distribution of aggregates in concrete.

The radius of the coarse, middle, and fine aggregate are 10, 5, and 2.5 mm, respectively, and the aggregate gradation is 5:3:2. Since there is very limited experimental data on the thickness and mechanical properties of the ITZ, in this study the thickness of ITZ is assumed to be 200 μm and its behavior described with the presented elasto-plastic-damage model with weaker mechanical properties as compared to the cement matrix.

It is noteworthy that due to the finite thickness of the ITZ in concrete, the cohesive zone modeling technique (e.g., [33,52]) which is suitable for interfaces of zero thickness is avoided in this study. Moreover, one of the major challenges in using the cohesive zone models is the identification of the associated material parameters. Therefore, with the lack of experimental data on the ITZ's traction-separation behavior, it will be a challenge to use the cohesive zone model to simulate the behavior of ITZ. However, the authors currently

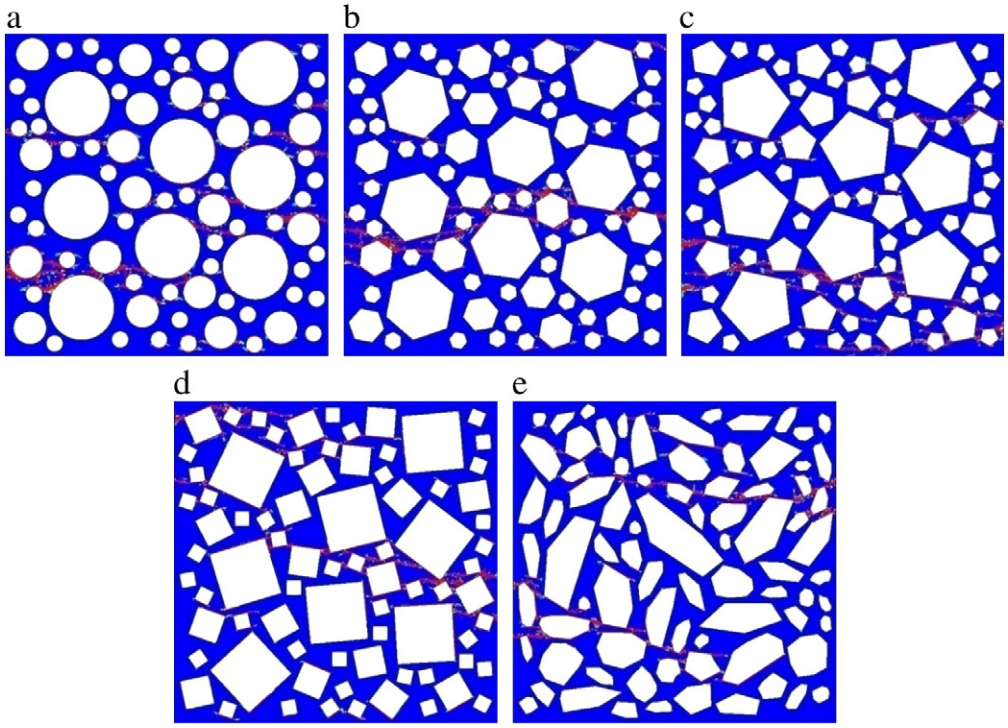

Fig. 4. Final micro-crack distributions for the aggregate shape effect analyses. (a) Circular, (b) hexagonal, (c) pentagonal, (d) tetragonal, (e) arbitrary polygonal shapes.

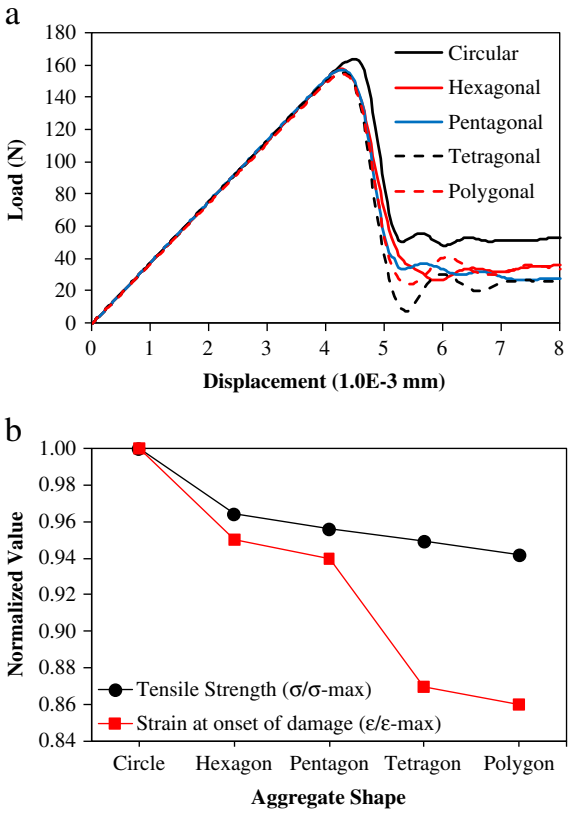

Fig. 5. Results of the aggregate shape effect analyses. (a) Load–displacement relation, (b) variation of the ultimate strength and the strain at onset of damage as a function of the aggregate shape.

investigating the comparisons between the current modeling technique of the ITZ and the cohesive zone modeling and the results will be reported in a future study.

4.1. Tensile and compressive material properties of the ITZ and mortar matrix

At mesoscopic level, it is crucial to understand the material mechanical properties and behavior of each phase and the interaction between the aggregate and the mortar matrix because the change in each material property has a great effect on the global macroscopic

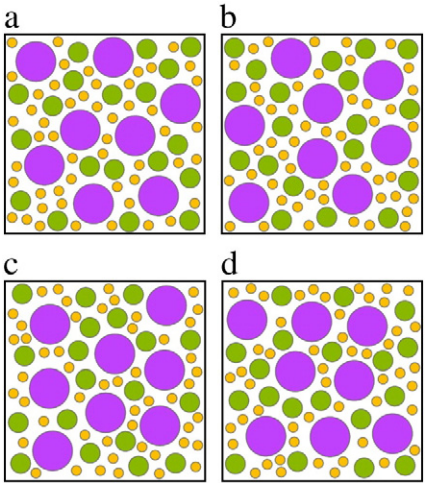

Fig. 6. Aggregate distribution sensitivity analyses with aggregate volume fraction of 50%. (a) Model 1, (b) model 2, (c) model 3, (d) model 4.

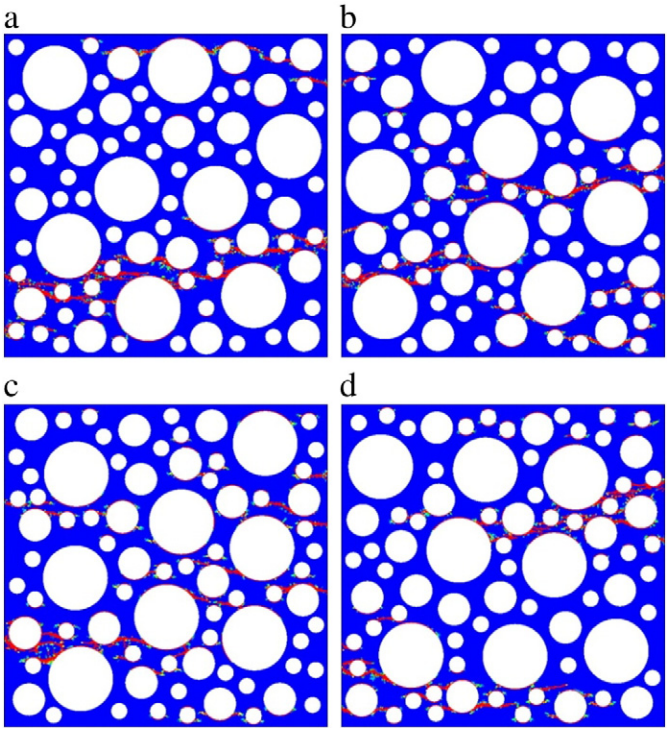

Fig. 7. Final micro-crack distributions for the aggregate distribution effect for (a) model 1, (b) model 2, (c) model 3, (d) model 4 shown in Fig. 6.

behavior of concrete. Because micro-cracks are initiated at the weakest link, where the ITZ is the weakest link, it is one of the most important tasks to define the tensile and compressive behavior of the ITZ for predicting the overall mechanical properties of concrete composites. However, it is difficult to determine the local mechanical properties of ITZ because of the complexity of their microstructure and the constraints of the existing measurement techniques [30,31,35,41]. Based on a systematic nano-indentation testing of the ITZ in concrete, Mondal et al. [31] have shown that the Young's modulus of the ITZ is comparable to the Young's modulus of the mortar matrix. However, they also showed through using electron microscopy imaging that the microstructure of the ITZ is highly heterogeneous and highly damaged due to pre-existence micro-voids and micro-cracks within this zone. Hence, one can assume that the tensile/compressive strength of the ITZ is weaker than that of the mortar matrix. Furthermore, the nano-indentation experimental data by Mondal et al. [31] has shown that there is no clear gradient of the mechanical properties across the ITZ thickness and the ITZ properties are heterogeneous. Thus, although the mechanical characteristic of the ITZ is not clearly understood currently, it can be assumed that the behavior of the ITZ, which has weaker

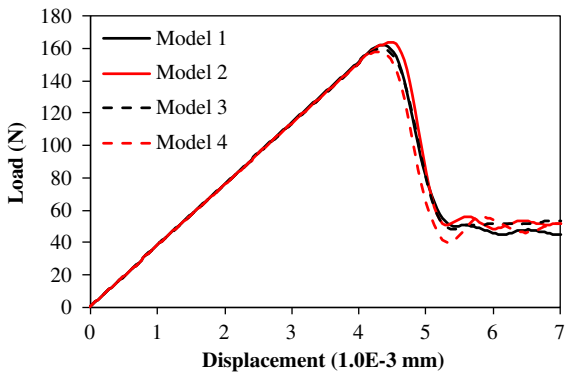

Fig. 8. Load–displacement relations for the different aggregate distributions in Fig. 6.

Table 2
The fraction of damaged elements for the different aggregate distributions in Fig. 6.

Model	1 (%)	2 (%)	3 (%)	4 (%)
ITZ	18.5	20.1	23.9	22.1
Mortar	2.7	2.5	2.3	2.1

mechanical properties [31,41], is similar to that of the mortar matrix and is homogenous across the ITZ's thickness. Based on this assumption, the material properties of the mortar matrix and the ITZ are chosen carefully such that the properties of the ITZ are chosen to be less than that of the mortar by a constant factor.

In this study, the presented coupled plasticity-damage model is adopted for modeling the tensile and compressive behavior of the ITZ and the mortar matrix, whereas the aggregate is modeled as a linear elastic material ($E=55{,}500$ MPa, $\nu=0.2$) since the aggregate shows a more brittle behavior than the mortar matrix, and has a higher Young's modulus and yield strength. It is noteworthy that the cyclic or uniaxial loading–unloading tensile and compressive stress–strain experimental curve should be used to identify unique values for the material parameters of the ITZ and the mortar matrix, such as $K_0^{\pm}$, $B^{\pm}$, $q^{\pm}$, h^{+}, b^{-}, and Q^{-}. The aim of this study, however, is not in predicting the behavior of a specific concrete structure. Therefore, the material constants of the ITZ and the matrix used in the analysis are assumed to show suitable tensile and compressive loading–unloading behavior based on the tensile and compressive loading–unloading experimental result by Taylor [43] and Karsan and Jirsa [19]. The material parameters used in the study are listed in Table 1, and the detailed calibration process of the material parameters can be found in Abu Al-Rub and Kim [2]. The predicted tensile and compressive stress–strain relations based on these material constants of the mortar matrix and ITZ are shown in Fig. 2.

4.2. The effect of aggregate shape

Currently, circular or spherical aggregate shape is commonly used for 2-D or 3-D meso-scale finite element analysis because of simplicity. However, it is found that the meso-scale concrete model using circular shape of aggregate tends to give higher strength compared to the model using irregular actual shape of aggregate [15]. This is attributed to the increased levels of stress concentration when modeling the actual shape of the aggregate. Therefore, the effect of the aggregate shape on the tensile strength of 2-D meso-scale concrete model is investigated in this section. Five different aggregate shapes; circular, hexagonal, pentagonal, tetragonal, and arbitrary polygonal shapes are considered as shown in Fig. 3.

Table 3
The number and fraction of aggregates used in the aggregate volume fraction simulations.

Volume fraction (%)	Coarse aggregate (%)	Middle aggregate (%)	Fine aggregate (%)	Total area (mm^2)	Actual volume fraction (%)
10	1 (31.4)	5 (39.3)	15 (29.5)	1001.38	10.01
20	3 (47.1)	8 (31.4)	21 (20.6)	1983.13	19.83
30	5 (52.4)	11 (28.8)	29 (19.0)	3004.15	30.04
40	6 (47.1)	17 (33.4)	40 (19.6)	4005.53	40.06
50	8 (50.3)	19 (29.8)	51 (20.0)	5006.92	50.07
60	10 (52.4)	22 (28.8)	60 (19.6)	6047.57	60.48

Micro-crack distribution for the aggregate shape sensitivity analyses at vertical displacement of 10 μm are shown in Fig. 4. Also, the corresponding load–displacement diagrams and the normalized values of the tensile strength and the strain capacity at the onset of damage are shown in Fig. 5. In this study, the strain at damage-onset is defined as the strain at which micro-cracks are initiated and degradation in strength and elastic modulus occurs. Therefore, by predicting this strain as a function of the material's microstructure, one can investigate the key microstructural parameters that mitigate damage onset and decreases cracking potential. It is obvious that the aggregate shape has a weak effect on the ultimate strength of concrete and on the strain to damage-onset as shown in Fig. 5, but significantly affects the crack initiation, propagation, and distribution as shown in Fig. 4. However, one can notice that due to the stress concentration at the sharp edges of polygonal aggregate shape, both the ultimate tensile strength and the strain at onset of damage of the circular shape aggregate model are higher than those of the other aggregate shapes. Specifically, the ultimate tensile strength of the circular aggregate model shows larger than 6% increase than that of the arbitrary polygonal shape aggregate model. The relatively small influence of aggregate shape on strength and strain at onset of damage is attributed to the fact that the simulations were conducted under tensile stresses. It is known that the influence of aggregate shape on concrete response is more evident under compressive loading stresses [29]. Therefore, in tension using different aggregate shapes by fixing their distribution does not affect the overall mechanical response significantly such that the behavior is completely dominated by the behavior of the cement paste and the ITZ.

Due to the small differences in the predictions of the overall tensile strength and strain capacity of the concrete when considering different

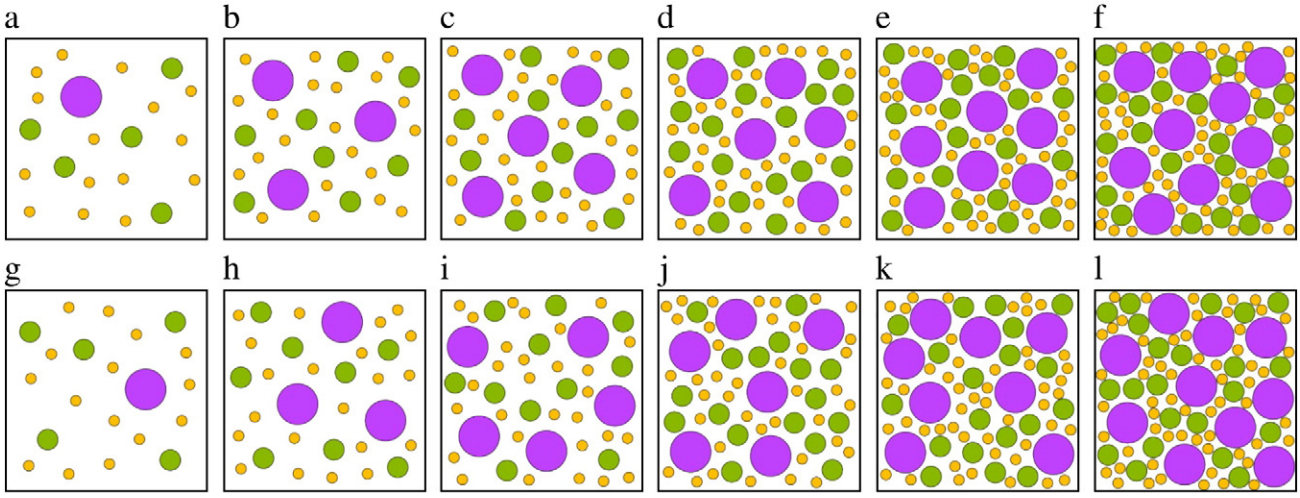

Fig. 9. Aggregate volume fraction sensitivity analysis models. (a) Set 1 — 10%, (b) set 1 — 20%, (c) set 1 — 30%, (d) set 1 — 40%, (e) set 1 — 50%, (f) set 1 — 60%, (g) set 2 — 10%, (h) set 2 — 20%, (i) set 2 — 30%, (j) set 2 — 40%, (k) set 2 — 50%, (l) set 2 — 60%.

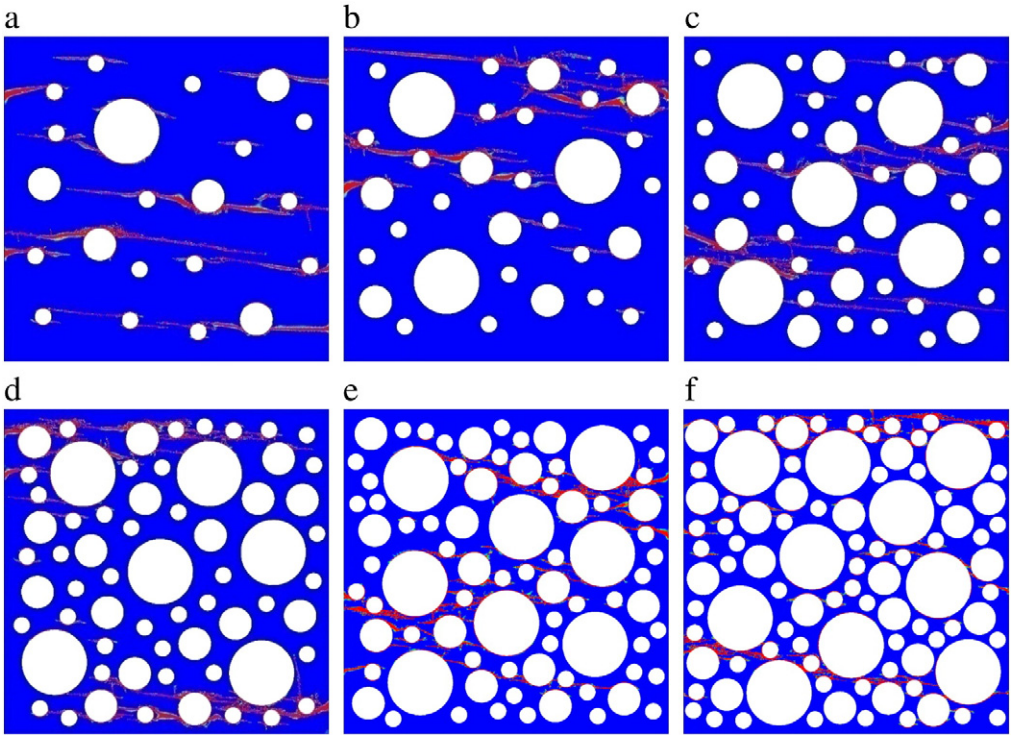

Fig. 10. Micro-crack distributions due to applied tensile loading for different aggregate volume fractions of set 1 in Fig. 9: (a) 10%, (b) 20%, (c) 30%, (d) 40%, (e) 50%, (f) 60%.

aggregate shapes, in the following simulations a circular aggregate shape is assumed for simplicity in carrying out the finite element simulations.

4.3. The effect of aggregate distribution

Although the maximum and minimum aggregate size and the aggregate gradation and volume fraction, depending on the purpose, can be controlled in the concrete mix design, it is actually impossible to control the distribution of aggregate. Furthermore, the concentration of the aggregates on a localized region due to poor mix or segregation may have effect on the strength of concrete. Mixing and pouring concrete is based on the basic assumption that aggregate is randomly and uniformly distributed, and the aggregate distribution has little effect on the strength and behavior of concrete. Therefore, the aggregate distribution effect is investigated in this section. Four different aggregate distributions are shown in Fig. 6. The size of the RVE is 100 mm × 100 mm, and the aggregate volume fraction of the models is identical with 50%. All aggregates are randomly distributed with the same aggregate gradation of 5:3:2.

The final micro-crack patterns and the load–displacement relations for the change of the aggregate distribution of the four simulated RVEs are shown in Figs. 7 and 8. As seen in Fig. 7, the micro-crack distribution is totally dependent on the distribution of aggregates. However, it is obvious from Fig. 8 that the tensile strength and strain capacity under tensile loading is less dependent on the aggregate distribution. This result can be explained with the global damage density, and the fraction of damaged element at 5 μm of vertical displacement as listed in Table 2. It can be seen from Table 2 that although the crack distribution of each model is quite different, the difference of the fraction of damaged elements is insignificant. Therefore, it can be concluded that the aggregate statistical distribution has a negligible effect on overall mechanical response of concrete composites.

4.4. The effect of aggregate volume fraction

It is obvious that aggregate plays a vital role in the fracture of concrete because aggregate takes up to 75% of the total volume of concrete, and the aggregate volume fraction is one of the most important factors governing the failure mechanism of concrete. It is well known through experimental tests that the Young's modulus of normal strength concrete is proportional to the aggregate volume fraction, whereas the compressive strength of concrete generally is inversely proportional to that [5,42]. However, there is little information

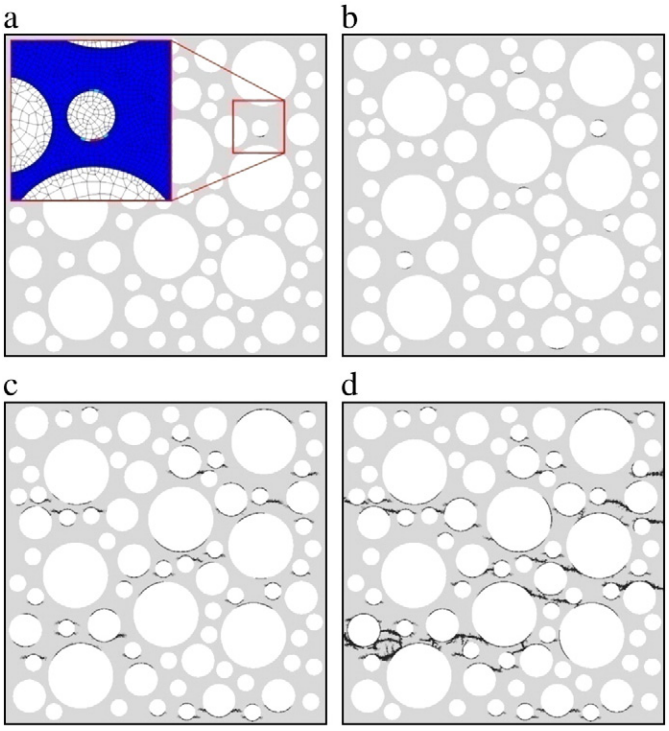

Fig. 11. Micro-crack nucleation and propagation for an RVE with aggregate volume fraction of 50%. Micro-crack distribution at increasing deformations of (a) 4.2 μm (onset of damage), (b) 4.5 μm (peak), (c) 5.0 μm, and (d) u = 10.0 μm.

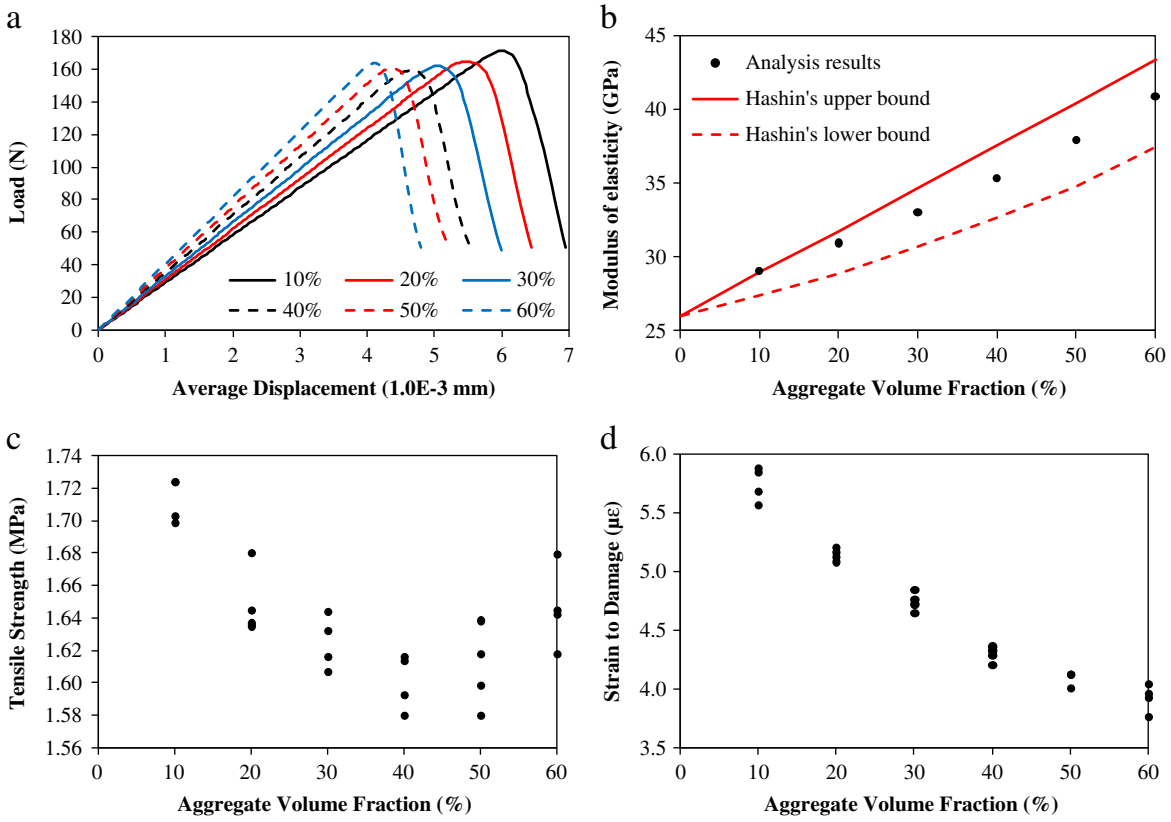

Fig. 12. Aggregate volume fraction on (a) load–displacement response, (b) Young's modulus, (c) tensile strength, and (d) strain at onset of damage.

how the aggregate volume fraction affects the tensile strength of concrete since the direct tensile test is not that easy to perform [41]. Therefore, the effect of the aggregate volume fraction on the tensile behavior of concrete is examined in this section.

In order to investigate the effect of aggregate volume fraction, Fig. 9 shows different RVEs with increasing aggregate volume fractions from 10% to 60%. The number and fraction of aggregates used in this analysis are summarized in Table 3. Each RVE in Fig. 9 is subjected to a vertical tensile displacement. However, Fig. 9(g–l) shows the same considered aggregate volume fractions, but with different aggregate distributions. This second set of RVEs are simulated in order to make sure that altering the aggregate distribution does not have significant effect on the drawn conclusions on the effects of aggregate volume fraction as concluded from the previous section. Also, it should be noted that the obtained results in this section are obtained from performing four simulations: (1) by applying tensile *vertical* displacement to the RVEs in *set 1* in Fig. 9(a–f); (2) by applying tensile *vertical* displacement to the RVEs in *set 2* in Fig. 9(g–l); (3) by applying tensile *horizontal* displacement to the RVEs in *set 1* in Fig. 9(a–f); and (4) by applying tensile *horizontal* displacement to the RVEs in *set 2* in Fig. 9(g–l). This is equivalent to simulating four different distributions for each considered aggregate volume fraction.

The micro-crack distributions at 0.02 mm of tensile vertical displacement are shown in Fig. 10. The crack distributions are totally dependent on the aggregate volume fraction and distribution, and tend to be more localized as the aggregate volume fraction increases. Furthermore, the process of micro-crack initiation and propagation is shown in Fig. 11. As seen, the tensile damage is initiated at the ITZ, the weakest region, which surrounds one of the fine aggregates at a vertical displacement of 4.2 μm. Subsequently, a number of micro-cracks develop at the ITZ regions simultaneously after damage initiation, and the micro-cracks are then propagate to the mortar matrix, coalesce with each other, and develop to macro-cracks as the vertical displacement increases.

The effects of varying the aggregate volume fraction on the overall mechanical response of the concrete composite are shown in Fig. 12. It can be seen from Fig. 12(b) that the Young's modulus of concrete is almost linearly proportional to the aggregate volume fraction and is not affected by the aggregate distribution. In addition, the results of the 2-D mesoscale analysis are compared with the Hashin's upper and lower bounds of the elastic moduli for three-phase composite material, and the results of RVEs are within the classical bounds of Hashin. It can also

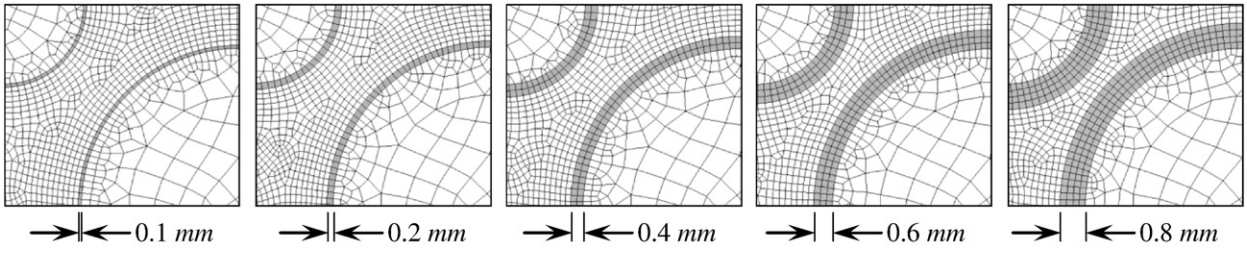

Fig. 13. Geometry and finite element meshes for studying the effect of varying the ITZ thickness.

be seen from Fig. 12(d) that the strain at the onset of damage is inversely proportional to the aggregate volume fraction and is not significantly influenced by the aggregate distribution. Whereas, the ultimate tensile strength of concrete as a function of aggregate volume fraction, unlike the Young's modulus and strain at damage initiation, is not monotonic such that the concrete capacity is found to be minimum at 40% volume fraction, and the analysis result is in good agreement with the experimental results by Stock et al. [41]. As can be seen from Fig. 12(c) that although the aggregate distribution has a slight effect on the tensile strength of concrete, the distribution of aggregates cannot be the reason for the observed response in Fig. 12(c). This observed behavior can be attributed to sever localized damage distribution leading to clear macro-crack evolution at the top and bottom of the 40% aggregate volume fraction RVE as shown in Fig. 10(d). Therefore, the load carrying capacity is mainly localized within small regions of the mortar matrix while the surrounding material is elastically unloaded. On the other hand, more distributed micro-damage evolution and propagation is seen for other volume fractions such that the loading carrying capacity is more distributed within the mortar matrix. Furthermore, it is believed that at volume fractions greater than 40% the aggregates are more closely packed to each other inducing confinement effects on the surrounding matrix and making the response stronger.

4.5. The effect of ITZ thickness

Understanding the characteristics of the ITZ is one of the most critical issues in predicting the overall mechanical response of concrete composites based on meso-scale simulations since the ITZ is the weakest region in concrete such that the strength and behavior of concrete is mainly governed by the properties of the ITZ (e.g. [30,31,41]). The ITZ as a constituent of concrete can be considered as an initial defect, and the increase of the ITZ thickness or volume may lower the global strength of concrete. The effect the ITZ thickness on the tensile strength of concrete is investigated in this section. Five thicknesses are simulated in this section as shown in Fig. 13. The thickness of the ITZ varies from 0.1 mm to 0.8 mm.

The ITZ thickness sensitivity analysis results are shown in Fig. 14. As shown in Fig. 14(a), the increase in the ITZ thickness has a slight effect on the post-peak behavior such that the brittleness of concrete increases as the ITZ thickness increases. However, as shown in Fig. 14(b) that the decrease in the tensile strength with increasing the thickness of the ITZ is not that significant and reaches a constant value with further increase in the ITZ thickness. This result indicates that further increase in the thickness of the ITZ may have no effect on the global strength of concrete. As seen in Fig. 14(c), the strain at onset of damage is not affected by increasing the ITZ thickness, whereas changing the aggregate volume fraction has a more significant effect on the strain to damage, which is the conclusion from the previous section.

Fig. 15 shows the micro-crack distribution for varying the ITZ thickness. Although the crack distribution and initiation points are almost the same for each change in the ITZ thickness, macro-cracks are more localized and wider as the thickness of the ITZ increases.

4.6. The effect of varying the strengths of the ITZ and mortar matrix

The global ultimate tensile strength of concrete as a function of the ITZ and mortar matrix tensile strengths is analyzed in this section. Although the ITZ strength cannot be in excess of the strength of mortar matrix for normal concrete, cases where the ITZ strength is higher than that of the mortar matrix are considered too. The ITZ strength may be greater than the matrix strength through surface treatment of aggregates and nano-modification of the cement paste (e.g. the use of nano-silica fume, nano-fibers, and nanotubes). In the following simulations, the reference tensile strengths (100% of strength) of the ITZ and mortar matrix are assumed to be 2.0 MPa and 3.0 MPa, respectively. The strength of the ITZ varies from 10% ($\sigma_{y-ITZ}=0.2$ MPa) to 200% ($\sigma_{y-ITZ}=4.0$ MPa) of the reference strength of ITZ, whereas the strength of the mortar matrix varies from 70% ($\sigma_{y-Mortar}=2.1$ MPa) to 200% ($\sigma_{y-Mortar}=6.0$ MPa) of the reference strength of matrix.

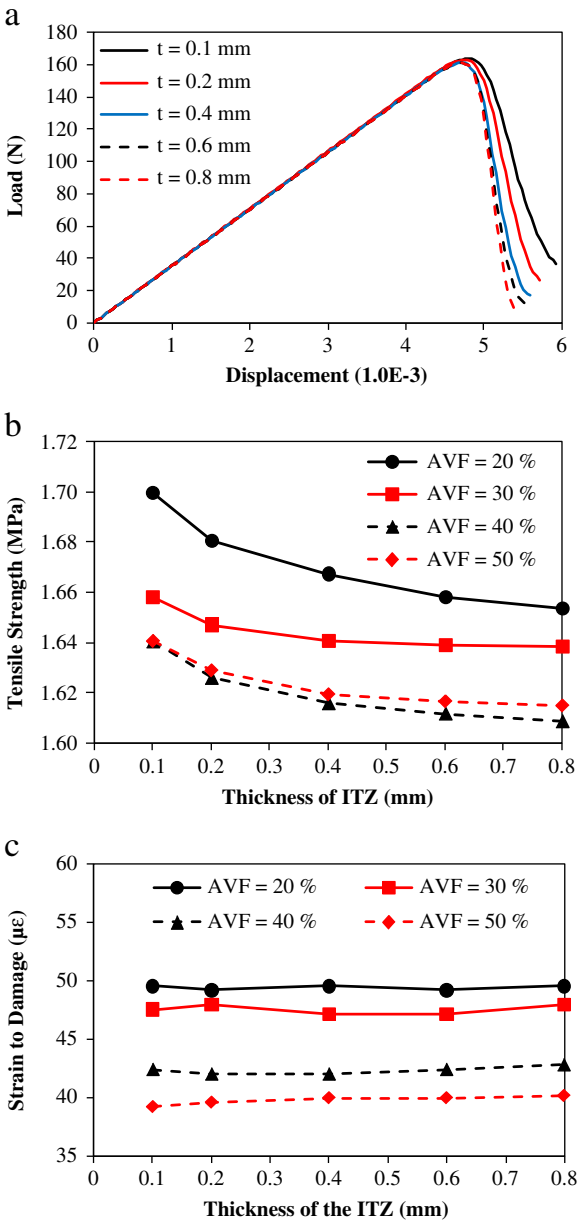

Fig. 14. The effect of varying the ITZ thickness on (a) the load–displacement relation for an aggregate volume fraction (AVF) of 40%, (b) the normalized tensile strength for different AVFs, and (c) the strain at onset of damage for different AVFs.

The analysis results of varying the ITZ and mortar matrix tensile strengths assuming 50% aggregate volume fraction is shown in Fig. 16. It can be seen from Fig. 16(a) that the variation in the ITZ strength has a significant effect on the global response of concrete. However, in case that the ITZ tensile strength is less than 40% of its reference strength (i.e. the ITZ tensile strength is equal or less than 0.8 MPa), the variation of the ITZ strength does not affect the ultimate tensile load as shown in Fig. 16(b). This is because the ITZ is easily damaged whereas the mortar matrix is still elastically loaded and can resist additional loading, which explains the observed subsequent hardening response in Fig. 16(b). Then, after the load is redistributed and transferred to the mortar matrix due to the complete damage of the ITZ region, one can start seeing micro-cracking of the mortar matrix. When the ITZ

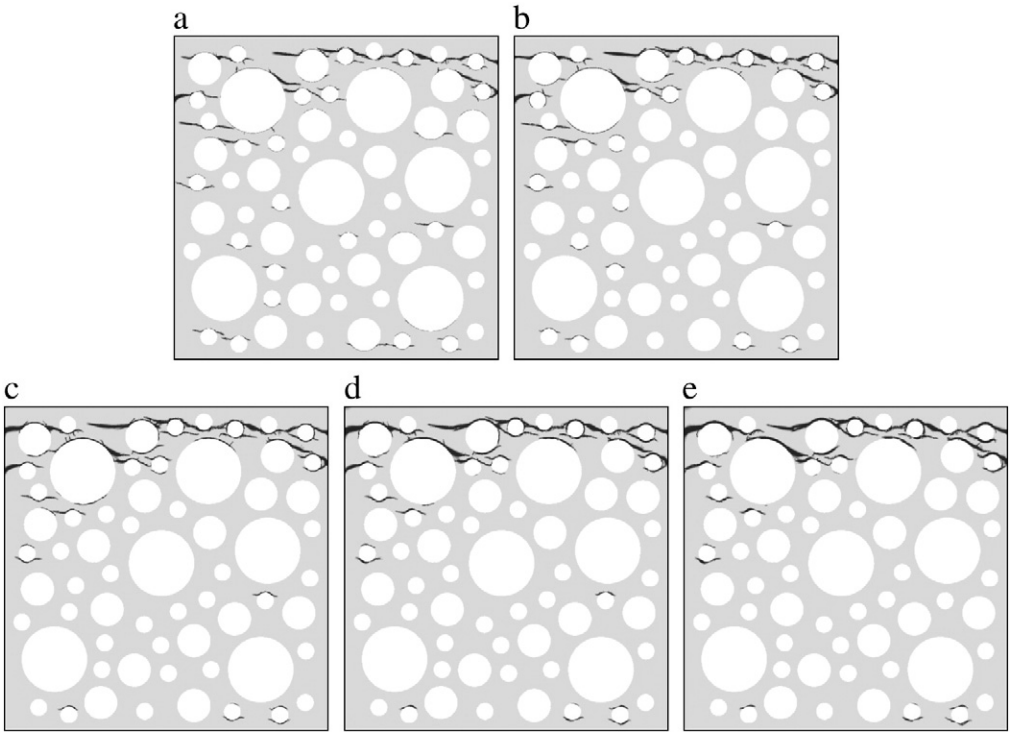

Fig. 15. Micro-crack distributions for ITZ thicknesses of (a) 0.1 mm, (b) 0.2 mm, (c) 0.4 mm, (d) 0.6 mm, and (e) 0.8 mm. The simulations are obtained at 6 μm displacement and for an aggregate volume fraction of 50%.

tensile strength lies in the range of 40% (0.8 MPa) and 150% (3.0 MPa) of its reference strength, the ultimate tensile strength of concrete increases linearly with the increase of the ITZ strength.

Fig. 17 shows the variation of micro-crack distributions as a function of the ITZ strength at 10 μm of applied vertical displacement. As seen, almost all ITZ elements are damaged when the strength of the ITZ is very low compared to the mortar matrix strength, and this distributed tensile damage on the ITZ yields higher ductility. As the ITZ strength increases, the more tensile cracks are propagated through the mortar matrix, and the model shows more brittle behavior. Also, one can notice from Fig. 17(a) and (b) that the majority of micro-cracking occurs at the ITZ region and much less within the mortar matrix as compared to the micro-crack distributions in Fig. 17(c–f). Therefore, increasing the ITZ strength will mitigate the micro-cracking from the interface (adhesive) to the matrix (cohesive), which leads to a stronger response as shown in Fig. 16. However, the additional increase in the ITZ strength over the mortar's strength has no effect on the ultimate strength of concrete because in this case the concrete strength is governed by the mortar's tensile strength of 3.0 MPa, which is the weakest link.

Although the variation of the ITZ strength influences the yield and the ultimate strength of concrete, the increase in the mortar matrix strength with assuming constant ITZ strength has no effect on the variation of the tensile strength of concrete. This is because the tensile strain at onset of damage at the ITZ is unchanged regardless of the increase in the mortar's strength due to the constant strength of the ITZ. Furthermore, the force resisted by the ITZ and aggregates is suddenly transmitted to the mortar matrix as the strain increases after damage initiation at the ITZ, and then the loss of the interaction between aggregates and mortar matrix due to the damage at the ITZ.

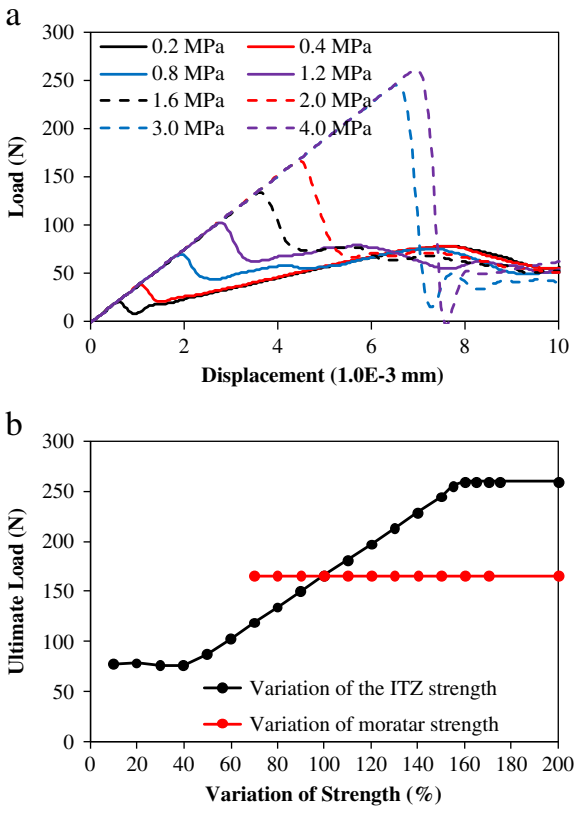

Fig. 16. The effect of varying the ITZ and mortar matrix tensile strengths on (a) the load–displacement response assuming $\sigma_{y-Mortar} = 3.0$ MPa, and (b) the ultimate load. 50% aggregate volume fraction is assumed.

5. 3-D meso-scale simulations

In order to use the proposed coupled plasticity-damage constitutive model for the comparison with the simplified 2-D meso-scale

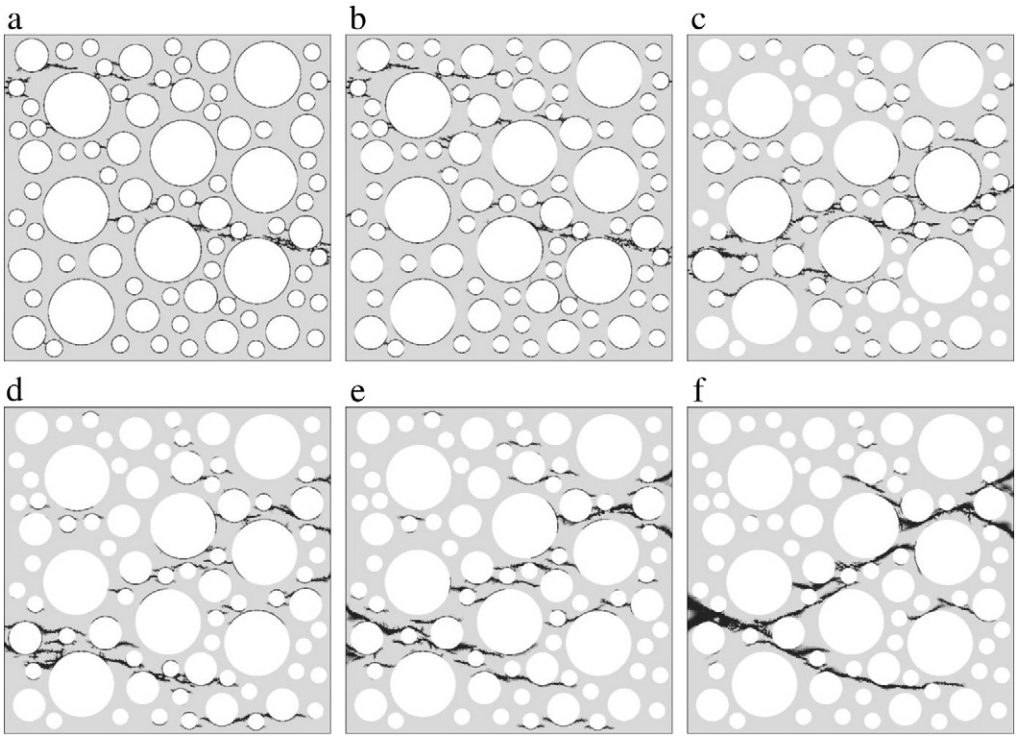

Fig. 17. Micro-crack distributions as a function of the ITZ strength for aggregate volume fraction of 50% and applied vertical displacement of 10 μm. (a) 10% (0.2 MPa), (b) 40% (0.8 MPa), (c) 70% (1.4 MPa), (d) 100% (2.0 MPa), (e) 130% (2.6 MPa), (f) 150% (3.0 MPa, same as the mortar strength).

analysis results, the tensile behavior of concrete is investigated with a 3-D meso-scale analysis model. Fig. 18 shows the 3-D meso-scale RVE of concrete, and the distribution of coarse, middle, and fine aggregates is shown in Fig. 19. In order to reduce the computational cost, only the size of the 3-D RVE is reduced to 50 mm × 50 mm × 50 mm, and all other micromechanical properties, such as the size of coarse, middle, and fine aggregates, the aggregate gradation, the ITZ thickness, and the material properties of the ITZ, aggregate, and mortar matrix are identical to those of the 2-D meso-scale analyses. A 40% of aggregate volume fraction is assumed for conducting the 3-D meso-scale analysis, and the number of coarse, middle, and fine aggregates used for the generation of the 3-D model is 6, 28, and 154, respectively. This 3-D simulation will show the applicability of the conducted 2-D simulations in that the later provide very meaningful simulations as compared to more realistic 3-D ones.

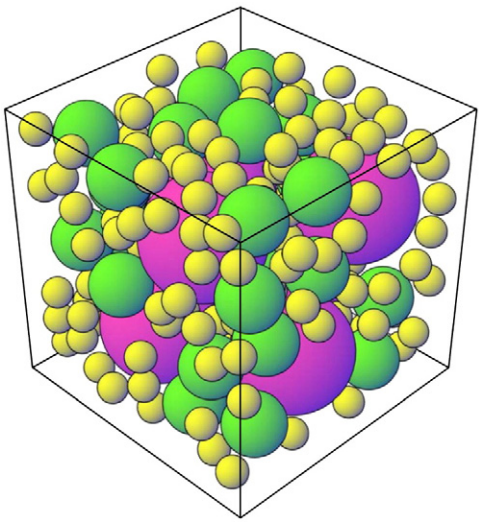

Fig. 18. 3-D meso-scale analysis model for concrete.

In order to compare the 3-D meso-scale analysis result with the corresponding 2-D simulations, another 2-D meso-scale analysis model which size and aggregate volume fraction are the same with that of the 3-D meso-scale analysis model is generated (Fig. 22(a)), and the stress–strain curve obtained from the 3-D meso-scale analysis model is compared with the 2-D meso-scale analysis result. As can be seen in Fig. 20, the 3-D analysis gives a lower ultimate tensile strength but a higher ductility compared to the 2-D meso-scale analysis. This is not only because they have totally different aggregate distribution but also because the ITZ volume fraction of the 3-D model is about 50% greater than that of the 2-D meso-scale model. However, the overall predicted responses from the 3-D and 2-D simulations are in good agreement which emphasize the validity of the conducted 2-D simulations.

The distribution of the tensile damage in the mortar matrix and the ITZ are shown in Fig. 21. Although the tensile damage is initiated at the ITZ when the tensile strain is 0.3×10^{-4}, the initial micro tensile damage at the ITZ has a marginal effect on the reduction of the Young's modulus of the concrete as shown in Fig. 20, and the Young's modulus of the 3-D meso-scale concrete analysis model begins to reduce when the tensile strain is 0.38×10^{-4} which is in agreement with the 2-D simulations. Due to the vertically applied tensile strain, the ITZ region at the top and bottom of aggregates is mainly damaged, and the damaged ITZ region is localized with forming a plane on the top part of the simulated 3-D micro-structure as shown in Fig. 21.

The process of the tensile damage propagation on the 2-D and 3-D meso-scale models with the increase of the tensile strain is compared in Fig. 22. For both cases, although the initial tensile damage occurs randomly at several locations simultaneously, the tensile damage is propagated with forming one or two overwhelming damaged planes as the tensile strain increases. Although there is slight discrepancy between the stress–strain curves (Fig. 20) and damage patters (Figs. 21 and 22) obtained from the 2-D and 3-D simulations, the 2-D meso-scale analysis also gives good prediction of the effect of the micromechanical

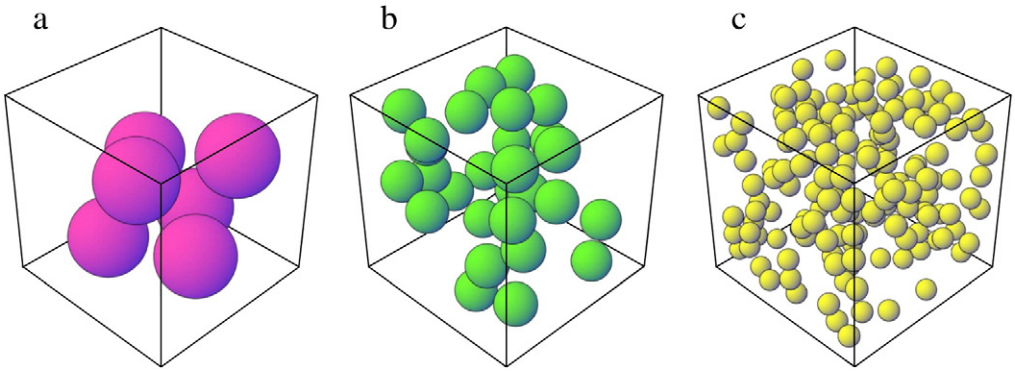

Fig. 19. Distribution of aggregates. (a) Coarse aggregates, (b) middle aggregates, and (c) fine aggregates.

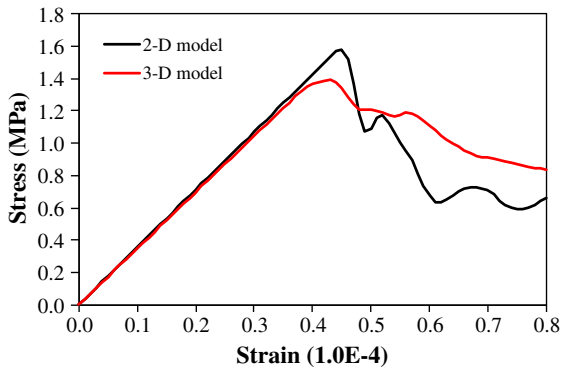

Fig. 20. Comparison between the 2-D and 3-D meso-scale overall stress–strain responses.

properties on the overall tensile behavior of concrete. Therefore, the presented 3-D simulation credits the conducted 2-D simulations as a valid approach to model the micro-structure of concrete.

Although the focus of the current paper is on 2-D description of the micro-structure of concrete in order to simulate their micro-damage evolution and predict their mechanical response, these simulations provide valuable and valid insights about the effect of concrete's micro-structure on the overall macroscopic properties of concrete composites. 3-D simulations with more realistic micro-structures are complex and computationally expensive, but at the same time provide conclusions and insights in good agreement with those from 2-D simulations. Moreover, the current presented computational framework can be used effectively in simulating the damage evolution in more complex and realistic 3-D micro-structure of concrete. The simulation results from more realistic 3-D concrete micro-structures based on images from X-ray tomography will be presented in a future work by the authors.

6. Conclusions

The effects of aggregate shape, statistical distribution, volume fraction, thickness of the ITZ, and the strength of the ITZ and mortar matrix on the overall macroscopic Young's modulus, tensile strength, and micro-crack initiation and propagation in normal plain concrete is thoroughly and systematically investigated in this study through using a coupled plasticity-damage model. The conclusions from the 2-D and 3-D meso-scale simulations of the concrete tensile behavior as a three-phase composite can be summarized as follows:

- Tensile damage is initiated first at the ITZ, the weakest region, and the stiffness of the 2-D meso-scale concrete model begins to be reduced as soon as damage is initiated such that cracks are propagated through the mortar matrix as load increases.
- The aggregate distribution effect can be neglected in the meso-scale analysis unless aggregates are severely clustered on a localized region.
- Due to the stress concentration at the sharp edges of polygonal shape of aggregates, both the ultimate tensile strength and the strain at onset of damage of the circular shape aggregate model are

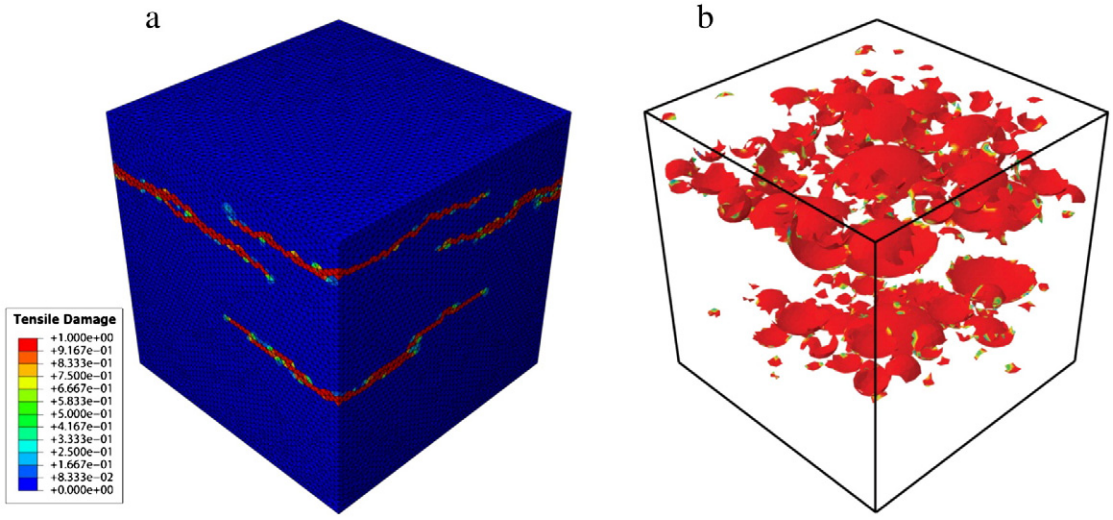

Fig. 21. Distribution of the tensile damage (a) within the mortar matrix, and (b) along the ITZ.

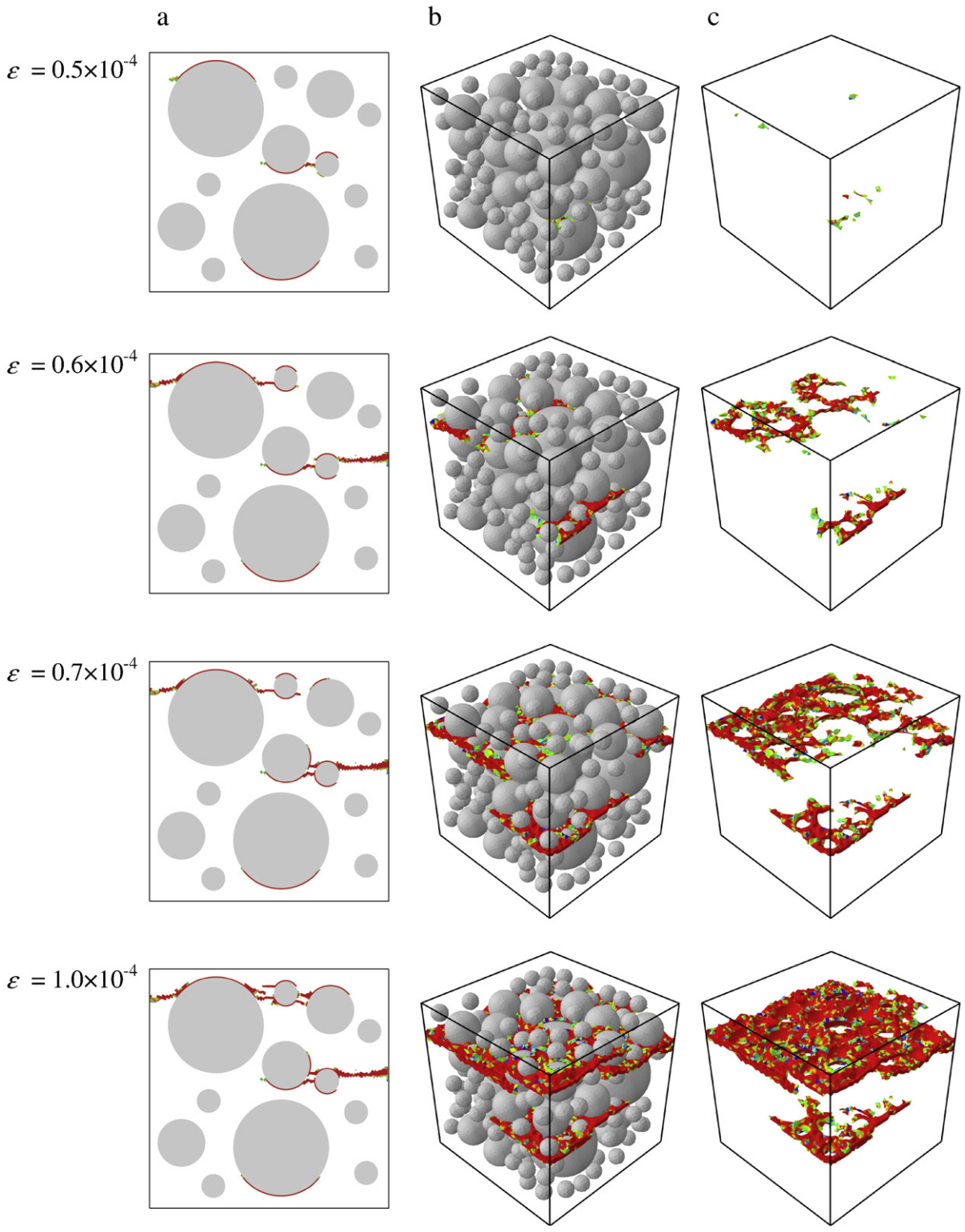

Fig. 22. Comparison of the tensile damage propagation at different applied tensile strain levels. (a) 2-D simulations, (b) 3-D simulations showing the aggregates, and (c) 3-D simulations without the aggregates.

higher than those of other aggregate shape models. It means that the meso-scale analysis using circular shape aggregate model may overestimate the strength of concrete.

- The Young's modulus of concrete is almost linearly proportional to the aggregate volume fraction while the ductility of concrete is inversely proportional to the aggregate volume fraction.
- Unlike Young's modulus and strain at damage initiation, the ultimate tensile strength of concrete due to change of aggregate volume fraction is not monotonic, where the concrete capacity is minimum at 40% volume fraction.
- The variation of the ITZ thickness has slight effect on the post-peak behavior such that the brittleness of concrete decreases and the

decrease rate of the strength is declined gradually as the ITZ thickness increases.
- The ultimate tensile strength of concrete increases linearly with the increase of the ITZ strength. However, the increase of the mortar matrix strength only with constant ITZ strength has no effect on the variation of the tensile strength of concrete.
- In case of the 3-D meso-scale analysis, the initial tensile damage at the ITZ doesn't provoke the yielding of the model, and the yielding is occurred as soon as the mortar matrix is damaged.
- The 3-D meso-scale simulations yield comparable results to the 2-D simulations. This credits the 2-D simulations as valid and useful in establishing the structure–property relationship for concrete.
- It is concluded that the aggregate volume fraction and the mechanical properties of the ITZ have significant effect on the overall mechanical response of concrete. Furthermore, there could be a specific aggregate volume fraction at which the tensile loading capacity of concrete is the minimum.

It is concluded that the presented micromechanical simulations provide valuable insights for relating the structure–property relationship in cementitious composites in order to ultimately guide the design of better concrete with enhanced tensile strength, fracture toughness, and ductility. Furthermore, the application of the presented computational framework for investigating the effects of fillers (e.g. micro- and nano-fibers, micro- and nano-inclusions) on the overall mechanical behavior of hardened cementitious composites will be investigated in a future work. Such detailed investigations are very difficult to perform through experimental routes and, therefore, the presented computational framework is highly desirable. Future study will also concentrate on studying the 2-D and 3-D mesoscopic behavior of concrete composite under various loading conditions with and without considering aggregate fracture. Also, application of the presented constitutive model and computational framework for conducting meso-scale simulations of more realistic 3-D concrete micro-structures based on 3-D images from X-ray computer tomography will be the focus of a future study.

Acknowledgment

Financial support by the Texas Southwest University Transportation Center (SWUTC) is gratefully acknowledged.

References

[1] ABAQUS Ver 6.5, Habbitt, Karlsson and Sorensen, Inc: Providence, RI.
[2] R.K. Abu Al-Rub, S.-M. Kim, Computational applications of a coupled plasticity-damage constitutive model for simulating plain concrete fracture, Engineering Fracture Mechanics 77 (2010) 1577–1603.
[3] R.K. Abu Al-Rub, G.Z. Voyiadjis, On the coupling of anisotropic damage and plasticity models for ductile materials, International Journal of Solids and Structures 40 (2003) 2611–2643.
[4] R.K. Abu Al-Rub, G.Z. Voyiadjis, A finite strain plastic-damage model for high velocity impacts using combined viscosity and gradient localization limiters, part I: theoretical formulation, International Journal of Damage Mechanics 15 (2006) 293–334.
[5] F.E. Amparano, Y. Xi, Y.S. Roh, Experimental study on the effect of aggregate content on fracture behavior of concrete, Engineering Fracture Mechanics 67 (2000) 65–84.
[6] Z.P. Bažant, M.R. Tabbara, M.T. Kazemi, G. Pijaudier-Cabot, Random particle model for fracture of aggregate or fiber composites, Journal of Engineering Mechanics 116 (8) (1990) 1686–1705.
[7] O. Bernard, F.J. Ulm, E. Lemarchand, A Multiscale micromechanics-hydration model for the early-age elastic properties of cement-based material, Cement and Concrete Research 33 (2003) 1293–1309.
[8] A. Caballero, C.M. López, I. Carol, 3D meso-structural analysis of concrete specimens under uniaxial tension, Computer Methods in Applied Mechanics and Engineering 195 (2006) 7182–7195.
[9] A. Caballero, I. Carol, C.M. López, 3D meso-mechanical analysis of concrete specimens under biaxial loading, Fatigue and Fracture of Engineering Materials and Structures 30 (2007) 877–886.
[10] L.Y. Chan, B. Andrawes, Characterization of the uncertainties in the constitutive behavior of carbon nanotube/cement composites, Science and Technology of Advanced Materials 10 (2009) 3–16.
[11] C.L. Chow, J. Wang, An anisotropic theory of elasticity for continuum damage mechanics, International Journal of Fracture 33 (1987) 2–16.
[12] U. Cicekli, G.Z. Voyiadjis, R.K. Abu Al-Rub, A plasticity and anisotropic damage model for plain concrete, International Journal of Plasticity 23 (2007) 1874–1900.
[13] J.P. Cordebois, F. Sidoroff, Anisotropic damage in elasticity and plasticity, Journal de Mécanique Théorique et Appliquée, Numero Special (1982) 45–60.
[14] V. Pensee, D. Kondo, L. Dormieux, Micromechanical analysis of anisotropic damage in brittle materials, ASCE Journal of Engineering Mechanics 128 (8) (2002) 889–897.
[15] C.B. Du, L.G. Sun, Numerical simulation of aggregate shapes of two-dimensional concrete and its application, Journal of Aerospace Engineering 20 (3) (2007) 172–178.
[16] G. Fu, W. Dekelbab, 3-D random packing of polydisperse particles and concrete aggregate grading, Powder Technology 133 (2003) 147–155.
[17] L.M. Kachonov, On the creep fracture time, Izv. Akad. Nauk USSR Otd. Tech 8 (1958) 26–31, (in Russian).
[18] B.L. Karihaloo, P.F. Shao, Q.Z. Xiao, Lattice modeling of the failure of particle composites, Engineering Fracture Mechanics 70 (2003) 2385–2406.
[19] I.D. Karsan, J.O. Jirsa, Behavior of concrete under compressive loadings, Journal of the Engineering Mechanics Division (ASCE) 95 (1969) 2535–2563.
[20] D. Krajcinovic, Damage Mechanics, North-Holland, Amsterdam, 1996.
[21] J. Kozicki, J. Tejchman, 2D lattice model for fracture in brittle materials, Archives of Hydro-Engineering and Environmental Mechanics 53 (2006) 137–154.
[22] A.K.H. Kwan, Z.M. Wang, H.C. Chan, Mesoscopic study of concrete II: nonlinear finite element analysis, Computers & Structures 70 (1999) 545–556.
[23] J. Lee, G.L. Fenves, A plastic-damage model for cyclic loading of concrete structures, Journal of Engineering Mechanics 124 (1998) 892–900.
[24] G. Lilliu, J.G.M. van Mier, 3D lattice type fracture model for concrete, Engineering Fracture Mechanics 70 (2003) 927–941.
[25] G. Lilliu, J.G.M. van Mier, On the relative use of micro-mechanical lattice analysis of 3-phase particle composites, Engineering Fracture Mechanics 74 (2007) 1174–1189.
[26] J.X. Liu, S.C. Deng, J. Zhang, N.G. Liang, Lattice type of fracture model for concrete, Theoretical and Applied Fracture Mechanics 48 (2007) 269–284.
[27] J.X. Liu, Z.Y. Zhao, S.C. Deng, N.G. Liang, Numerical investigation of crack growth in concrete subjected to compression by the generalized beam lattice model, Computer Mechanics 43 (2009) 277–295.
[28] J. Lubliner, J. Oliver, S. Oller, E. Onate, A plastic-damage model for concrete, International Journal of Solids and Structures 25 (1989) 299–326.
[29] E. Masad, L. Tashman, D. Little, H. Zbib, Viscoplastic modeling of asphalt mixes with the effects of anisotropy, damage and aggregate characteristics, Mechanics of Materials 37 (12) (2005) 1242–1256.
[30] P. Mondal, S.P. Shah, L.D. Marks, Nano-scale characterization of cementitious materials, ACI Materials Journal 105 (2008) 174–179.
[31] P. Mondal, S.P. Shah, L.D. Marks, Nanomechanical properties of interfacial transition zone in concrete, Proceedings of Nanotechnology in Construction 3, Springer, 2009, pp. 315–320.
[32] S. Murakami, N. Ohno, A continuum theory of creep and creep damage, Proceedings of the Third IUTAM Symposium on Creep in Structures, Springer, Berlin, 1981, pp. 422–444.
[33] A. Needleman, An analysis of decohesion along an imperfect interface, International Journal of Fracture 40 (1990) 21–40.
[34] B. Pichler, C. Hellmich, J. Eberhardsteiner, "Spherical and acicular representation of hydrates in a micromechanical model for cement paste- prediction of early-age elasticity and strength,, Acta Mechanica 203 (2009) 137–162.
[35] G. Ramesh, E.D. Sotelino, W.F. Chen, Effect of transition zone on elastic stresses in concrete materials, J. Mater. Civil Eng. 10 (1998) 275–282.
[36] J. Sanahuja, L. Dormieus, G. Chanvillard, Modelling elasticity of a hydrating cement paste, Cement and Concrete Research 37 (2007) 1427–1439.
[37] E. Schlangen, E.J. Garbocai, Fracture simulations of concrete using lattice model: computational aspect, Engineering Fracture Mechanics 57 (2/3) (1997) 319–322.
[38] K.L. Scrivener, A.K. Crumbie, P. Laugesen, The interfacial transition zone (ITZ) between cement paste and aggregate in concrete, Interface Science 12 (2004) 411–421;
J.C. Simo, T.J.R. Hughes, Computational Inelasticity: Interdisciplinary Applied Mathematics, Springer, New York, 1998.
[39] J.C. Simo, J.W. Ju, Strain and stress-based continuum damage model. Part I: formulation, International Journal of Solids and Structures 23 (1987) 821–840.
[40] J.C. Simo, J.W. Ju, Strain- and stress-based continuum damage models. Part II: computational aspects, International Journal of Solids and Structures 23 (1987) 841–869.
[41] A.F. Stock, D.J. Hannant, R.I.T. Williams, The effect of aggregate concentration upon the strength and modulus of elasticity of concrete, Magazine of Concrete Research 31 (109) (1979) 225–234.
[42] M.A. Tasdemir, B.L. Karihaloo, Effect of aggregate volume fraction on the fracture parameters of concrete: a meso-mechanical approach, Magazine of Concrete Research 53 (6) (2001) 405–415.
[43] R.L. Taylor, FEAP: a finite element analysis program for engineering workstation, (Draft version), Rep. No. UCB/SEMM-92Department of Civil Engineering, University of California, Berkeley, 1992.
[44] J.G.M. van Mier, Fracture Processes of Concrete: Assessment of Material Parameters for Fracture Model, CRC Press, Boca Raton, Fla, 1997.
[45] G.Z. Voyiadjis, T. Park, Anisotropic damage effect tensors for the symmetrization of the effective stress tensor, Journal of Applied Mechanics, ASME 64 (1997) 106–110.
[46] G.Z. Voyiadjis, P.I. Kattan, Advances in Damage Mechanics: Metals and Metals Matrix Composites, Elsevier, Oxford, 1999.

[47] G.Z. Voyiadjis, R.K. Abu Al-Rub, A.N. Palazotto, Non-Local coupling of viscoplasticity and anisotropic viscodamage for impact problems using the gradient theory, Archives of Mechanics 55 (2003) 39–89.
[48] G.Z. Voyiadjis, R.K. Abu Al-Rub, A.N. Palazotto, Thermodynamic framework for coupling of non-local viscoplasticity and non-local anisotropic viscodamage for dynamic localization problems using gradient theory, International Journal of Plasticity 20 (2004) 981–1038.
[49] Z.M. Wang, A.K.H. Kwan, H.C. Chan, Mesoscopic study of concrete II: nonlinear finite element analysis, Computers & Structures 70 (1999) 545–556.
[50] F.H. Wittmann, P.E. Roelfdtra, H. Sadouki, Simulation and analysis of composite structures, Material Science Engineering 68 (1984) 239–248.
[51] P. Wriggers, S.O. Moftah, Mesoscale models for concrete: homogenisation and damage behavior, Finite Elements in Analysis and Design 42 (2006) 623–636.
[52] X.P. Xu, A. Needleman, Numerical simulations of fast crack growth in brittle solids, Journal of the Mechanics and Physics of Solids 42 (1994) 1397–1434.
[53] D.H. Zhang, J.B. Xing, F.S. Zhu, Study of failure process in concrete samples by using numerical simulation, Journal of Northeastern University 25 (2) (2004) 175–178, (in Chinese).
[54] Q.Z. Zhu, D. Kondo, J.F. Shao, Homogenization-based analysis of anisotropic damage in brittle materials with unilateral effect and interactions between microcracks, Int. J. Numer. Anal. Meth. Geomech. 33 (6) (2009) 749–772.
[55] J. Lemaitre, J.-L. Chaboche, Mechanics of Solid Materials, Cambridge University Press, Cambridge, UK (1990).